



8-1999

## Titanium nitride and silicon nitride films grown by pulsed laser deposition

Won-Seok Kim

Follow this and additional works at: [https://trace.tennessee.edu/utk\\_gradthes](https://trace.tennessee.edu/utk_gradthes)

---

### Recommended Citation

Kim, Won-Seok, "Titanium nitride and silicon nitride films grown by pulsed laser deposition. " Master's Thesis, University of Tennessee, 1999.  
[https://trace.tennessee.edu/utk\\_gradthes/9880](https://trace.tennessee.edu/utk_gradthes/9880)

This Thesis is brought to you for free and open access by the Graduate School at TRACE: Tennessee Research and Creative Exchange. It has been accepted for inclusion in Masters Theses by an authorized administrator of TRACE: Tennessee Research and Creative Exchange. For more information, please contact [trace@utk.edu](mailto:trace@utk.edu).

To the Graduate Council:

I am submitting herewith a thesis written by Won-Seok Kim entitled "Titanium nitride and silicon nitride films grown by pulsed laser deposition." I have examined the final electronic copy of this thesis for form and content and recommend that it be accepted in partial fulfillment of the requirements for the degree of Master of Science, with a major in Metallurgical Engineering.

Anthony J. Pedraza, Major Professor

We have read this thesis and recommend its acceptance:

George M. Pharr, Douglas H. Lowndes, David C. Joy

Accepted for the Council:

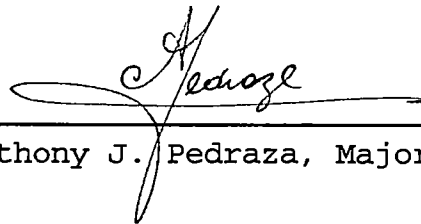
Carolyn R. Hodges

Vice Provost and Dean of the Graduate School

(Original signatures are on file with official student records.)

To the Graduate Council:

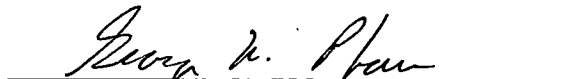
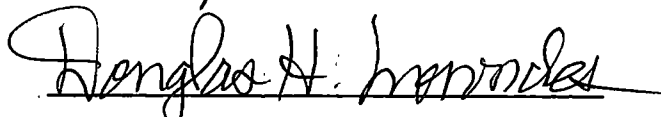
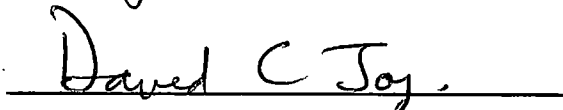
I am submitting herewith a thesis written by Won-Seok Kim entitled "Titanium Nitride and Silicon Nitride Films Grown by Pulsed Laser Deposition". I have examined the final copy of this thesis for form and content and recommend that it be accepted in partial fulfillment of the requirements for the degree of Master of Science with a major in Metallurgical Engineering.



Anthony J. Pedraza, Major Professor

We have read this thesis

And recommend its acceptance:

Accepted for the Council:



Associate Vice Chancellor

and Dean of the Graduate School

**TITANIUM NITRIDE AND SILICON NITRIDE  
FILMS GROWN BY PULSED LASER DEPOSITION**

A Thesis

Presented for the

Master of Science

Degree

The University of Tennessee, Knoxville

WON-SEOK KIM

August, 1999

## DEDICATION

This thesis is dedicated to my parents, Soon-Il Kim and Chyun-Nyum Hyun, who have always been a paragon of my life and a source of encouragement and strength.

I also dedicate this thesis to my sibling and their family, who have supported and inspired me.

## ACKNOWLEDGMENTS

I wish to thank my major professor, Dr. Anthony J. Pedraza, for his countless advice and support for the last two years. I also wish to thank Dr. Douglas H. Lowndes for support and for his efforts as my thesis committee. I would like to thank Dr. George M. Pharr for his mechanical test of samples and for serving on one of my thesis committee members. I also would like to thank Dr. David C. Joy for teaching me the joys of electron microscopies and for guidance as my thesis committee.

I wish to thank my fellow graduate students, Mr. Jason Fowlkes, for his help in the use of the laser and SEM work, Mr. Jeongguk Kim, for his advice and encouragement throughout this thesis work. Ms. Hee-Jeong Im at Chemistry Department deserves my thanks for her help in the use of XPS.

I thank Mr. Douglas Fielden and Mr. Larry Smith in the department machine shop for making our deposition chamber assembly and solving lots of mechanical problem. My thanks are extended to Mr. Frank Holiway and Mr. Randy Stooksbury for supply laboratory materials and instrument for this thesis work.

## ABSTRACT

Titanium nitride, silicon nitride, and their multi-layered films grown on Si(100) by Pulsed Laser Deposition (PLD) have been studied. The crystal structure and orientation of films were investigated by XRD and TEM. Titanium nitride film produced at room temperature was a polycrystal with 0.426 nm lattice constant whereas silicon nitride film grown at same condition was the amorphous. Particulates, one of the disadvantages of the PLD technique, were examined in the silicon nitride films varying the laser energy density, the repetition rate, and the target-substrate distance. The effect of laser ablation on the target was studied by SEM and XPS. The silicon nitride target after ablation for 25,000 pulses at  $E_d = 2.5 \text{ J/cm}^2$  produced nitrogen-deficient cones that were aligned along the direction of the incident laser beam. The hardness and elastic modulus of the films grown at room temperature in vacuum and at 500 °C in nitrogen background gas ( $10^{-3}$  torr) were determined using the Nano Indenter®II. The highest hardness and elastic modulus in this study were obtained from the TiN film grown at room temperature in vacuum: 26.44 GPa and 265 GPa, respectively. Multi-layered

films consisting of titanium nitride and silicon nitride films had intermediate hardness values. Titanium nitride and silicon nitride film grown at different temperature and pressure were examined by XPS to determine the effect of nitrogen content in films on the hardness. The more nitrogen the higher the hardness for both titanium nitride and silicon nitride films, regardless of deposition temperature.



## TABLE OF CONTENTS

CHAPTER	PAGE
1. INTRODUCTION.....	1
2. LITERATURE RIVIEW.....	4
2.1 Pulsed laser Deposition.....	4
2.1.1 Principle of Excimer Laser.....	4
2.1.2 Basics of PLD.....	7
2.1.3 Film Growth Modes.....	7
2.1.4 Advantages of PLD.....	11
2.1.5 Disadvantages of PLD.....	12
2.2 Hard Coatings.....	22
2.2:1 Hard Materials for Coating.....	22
2.2.2 Hardening Mechanism in Coatings.....	26
2.2.3 Nanocrystalline Transition Metal Nitrides / Amorphous Silicon Nitride Composite Materials.....	30
2.3 Mechanical Properties of Hard Coatings.....	33
2.3.1 Hardness and Elastic Modulus.....	33
2.3.2 Internal Stresses of the Coatings.....	38
3. EXPERIMENTAL PROCEDURE.....	41
3.1 Materials Used.....	41

3.2 Deposition Process.....	41
3.3 Analysis of Coatings.....	44
3.3.1 X-ray Diffraction.....	44
3.3.2 Transmission Electron Microscopy.....	44
3.3.3 Scanning Electron Microscopy.....	45
3.3.4 X-ray Photoelectron Spectroscopy.....	45
3.3.5 Nanoindentation.....	46
<b>4. RESULTS AND DISCUSSION.....</b>	<b>50</b>
4.1 X-ray Diffraction of Titanium Nitride and Silicon Nitride Films.....	50
4.2 Transmission Electron Microscopy.....	53
4.3 Particulates of Silicon Nitride Film.....	60
4.4 Effect of Laser Ablation on Targets.....	73
4.5 Hardness and Elastic Modulus of Titanium Nitride Film and Silicon Nitride Film.....	80
<b>5. CONCLUSIONS.....</b>	<b>103</b>
<b>REFERENCES.....</b>	<b>107</b>
<b>VITA.....</b>	<b>112</b>

## LIST OF TABLES

TABLES	PAGE
2.1 Primary reaction channels for KrF excimer.....	5
2.2 Properties of hard materials.....	25
3.1 Indentation test segments used.....	49
4.1 The hardness and elastic modulus of multi-layered films.....	101
4.2 Mechanical properties of films obtained.....	102

## LIST OF FIGURES

FIGURE	PAGE
2.1 Electron states in excimer emission.....	6
2.2 Schematic diagram of a PLD apparatus.....	8
2.3 Film growth modes; (a) Frank-van der Merwe, (b) Volmer-Weber, and (c) Stranski-Krastanov.....	10
2.4 The number of particulates corrected for the film thickness vs. the laser energy density in YBCO films produced by XeCl laser ablation.....	15
2.5 SEM micrographs of PLD thin films with a peak power of 0.79 GW/cm <sup>2</sup> : (a) 266 nm, 9000 pulses; (b) 355 nm, 9000 pulses; (c) 533 nm, 15000 pulses; (d) 1064 nm, 15000 pulses. Scale marker; 1 μm.....	16
2.6 Cumulative size distribution of ultrafine Fe particulates made under Ar pressure of 0.1, 1.3, 13.3, & 200 kpa.....	18
2.7 Deposition geometry.....	20
2.8 Factors affecting coated materials properties.....	23
2.9 Hardness of polycrystalline superlattice films of TiN/NbN, TiN/VN, and NbN/VN as a function of the superlattice period.....	29

2.10 Suggested microstructure of the superhard nanocrystalline composite showing the propagation of nanocracks, which may form under applied stress, is hindered.....	32
2.11 A schematic diagram of a cross-section through an indentation.....	36
2.12 A schematic diagram of load vs. displacement showing the contact depth.....	37
2.13 Sequence of events leading to	
(a) residual tensile stress in film,	
(b) residual compressive stress in film.....	39
3.1 A Schematic diagram of PLD apparatus at the Laser Processing Laboratory, UT.....	42
3.2 A schematic diagram of the experimental apparatus used to perform the indentation experiments:	
(A) sample; (B) indenter; (C) load application coil; (D) indentation column guide spring;	
(E) capacitive displacement sensor.....	48
4.1 XRD of a TiN target(a) and a TiN film(b) deposited at $E_d = 2.86 \text{ J/cm}^2$ .....	51
4.2 XRD for (200) plane of a TiN target(a) and a TiN film(b) deposited at $E_d = 2.86 \text{ J/cm}^2$ .....	52
4.3 XRD of a $\text{Si}_3\text{N}_4$ target(a) and a $\text{Si}_3\text{N}_4$ film(b)	

deposited at $E_d = 3 \text{ J/cm}^2$ .....	54
4.4 SAD of a TiN film (a) and a $\text{Si}_3\text{N}_4$ film (b) deposited at $E_d = 2.5 \text{ J/cm}^2$ .....	56
4.5 Bright field image (a) and EDS (b) of a TiN film (40 nm) deposited at $E_d = 2.5 \text{ J/cm}^2$ .....	57
4.6 Bright field image (a) and EDS (b) of a $\text{Si}_3\text{N}_4$ (40 nm) + TiN (10 nm) multilayer film deposited at $E_d = 2.5 \text{ J/cm}^2$ .....	58
4.7 Bright field image (a) and EDS (b) of a $\text{Si}_3\text{N}_4$ (40 nm) + TiN (20 nm) multilayer film deposited at $E_d = 2.5 \text{ J/cm}^2$ .....	59
4.8 SEM micrograph of a silicon nitride film deposited for 5000 pulses at $E_d = 1.8 \text{ J/cm}^2$ . The repetition rate was 10 Hz and the target-substrate distance was 4 cm.....	61
4.9 SEM micrograph of a silicon nitride film deposited for 5000 pulses at $E_d = 2.5 \text{ J/cm}^2$ . The repetition rate was 10 Hz and the target-substrate distance was 4 cm .....	62
4.10 SEM micrograph of a silicon nitride film deposited for 5000 pulses at $E_d = 3.15 \text{ J/cm}^2$ . The repetition rate was 10 Hz and the target-substrate distance was 4 cm.....	63
4.11 SEM micrograph of a silicon nitride film	

	deposited for 5000 pulses at $E_d = 2.5 \text{ J/cm}^2$ .	
	The target-substrate was 20 Hz and	
	the substrate-target distance was 4 cm.....	65
4.12	SEM micrograph of a silicon nitride film	
	deposited for 5000 pulses at $E_d = 2.5 \text{ J/cm}^2$ .	
	The repetition rate was 30 Hz and	
	the target-substrate was 4 cm.....	66
4.13	SEM micrograph of a silicon nitride film	
	deposited for 5000 pulses at $E_d = 2.5 \text{ J/cm}^2$ .	
	The repetition rate was 10 Hz and	
	the target-substrate distance was 2 cm.....	68
4.14	SEM micrograph of a silicon nitride film	
	deposited for 5000 pulses at $E_d = 2.5 \text{ J/cm}^2$ .	
	The repetition rate was 10 Hz and	
	the target-substrate distance was 5 cm.....	69
4.15	SEM micrograph of a silicon nitride film	
	deposited for 5000 pulses at $E_d = 2.5 \text{ J/cm}^2$ .	
	The repetition rate was 10 Hz and	
	the target-substrate distance was 6 cm.....	70
4.16	Deposition rate as a function of	
	the target-substrate distance	
	for 5000 pulses at $E_d = 2.5 \text{ J/cm}^2$ .	
	The repetition rate was 10 Hz.....	72
4.17	SEM morphology of the titanium nitride	

target polished(a) and ablated(b) for 25,000 pulses at $E_d = 2.5 \text{ J/cm}^2$ .....	74
4.18 SEM morphology of the silicon nitride target after being ablated for 25,000 pulses at $E_d = 2.5 \text{ J/cm}^2$ .....	75
4.19 A Dektak II profilometer of the silicon nitride target being ablated for 25000 pulses at $E_d = 2.5 \text{ J/cm}^2$ .  The vertical scale is in micrometer and the horizontal scale is Angstrom.....	77
4.20 XPS survey spectrum of  the polished silicon nitride target(a) and the ablated silicon nitride target(b) for 25,000 pulses at $E_d = 2.5 \text{ J/cm}^2$ .....	78
4.21 Hardness as a function of contact depth for films deposited at $E_d = 2.5 \text{ J/cm}^2$ .  The repetition rate was 20 Hz and the target-substrate distance was 4 cm.  The depositions were performed at room temperature in vacuum.....	81
4.22 Elastic modulus as a function of contact depth for films deposited at $E_d = 2.5 \text{ J/cm}^2$ .  The repetition rate was 20 Hz and the target-substrate distance was 4 cm.	



The depositions were performed at room temperature in vacuum.....	83
4.23 Hardness as a function of contact depth for films deposited at $E_d = 2.5 \text{ J/cm}^2$ . The repetition rate was 20 Hz and the target-substrate distance was 4 cm. The depositions were performed at 500 °C in nitrogen atmosphere ( $1 \sim 2 * 10^{-3} \text{ torr}$ ).....	85
4.24.(a) XPS survey spectrum of the titanium nitride film deposited with $E_d = 2.5 \text{ J/cm}^2$ at room temperature in vacuum. The repetition rate was 20 Hz and the target-substrate distance was 4 cm.....	87
4.24.(b) XPS survey spectrum of the titanium nitride film deposited with $E_d = 2.5 \text{ J/cm}^2$ at 500 °C in $\text{N}_2$ ( $1 \sim 2 * 10^{-3} \text{ torr}$ ). The repetition rate was 20 Hz and the target-substrate was 4 cm.....	88
4.25 XRD of silicon nitride film deposited with $E_d = 2.5 \text{ J/cm}^2$ at room temperature in vacuum(a) and XRD of silicon nitride film deposited with $E_d = 2.5 \text{ J/cm}^2$ at 500 °C in nitrogen atmosphere(b) ( $1 \sim 2 * 10^{-3} \text{ torr}$ ).....	90

4.26.(a) XPS survey spectrum of the silicon nitride film deposited with $E_d = 2.5 \text{ J/cm}^2$ at room temperature in vacuum. The repetition rate was 20 Hz and the target-substrate distance was 4 cm.....	91
4.26.(b) XPS survey spectrum of the silicon nitride film deposited with $E_d = 2.5 \text{ J/cm}^2$ at 500 °C in $\text{N}_2$ ( $1 \sim 2 * 10^{-3}$ torr ). The repetition rate was 20 Hz and the target-substrate was 4 cm.....	92
4.27 Elastic modulus as a function of contact depth for films deposited at $E_d = 2.5 \text{ J/cm}^2$ . The repetition rate was 20 Hz and the target-substrate distance was 4 cm. The depositions were performed at 500 °C in nitrogen atmosphere ( $1 \sim 2 * 10^{-3}$ torr ).....	94
4.28 Micrographs of silicon nitride film deposited with $E_d = 2.5 \text{ J/cm}^2$ at room temperature in vacuum(a) and at 500 °C in nitrogen atmosphere ( $1 \sim 2 * 10^{-3}$ torr ) (b).....	99

## CHAPTER 1

### INTRODUCTION

Pulsed laser deposition (PLD) has been widely used to produce a variety of films such as high temperature superconducting oxide films, hard diamond-like carbon films, and epitaxial thin films. The advantage of PLD lies in its simple implementation, near stoichiometric deposition from multicomponent targets at relatively low temperatures. Application of PLD has been extended to hard coatings due to the possibility of formation of films on substrates having no thermal damage since deposition is made at low substrate temperatures, and the easiness of controlling process parameters to maximize the quality of films.

Titanium nitride films and coatings have several applications as hard and wear resistant coatings, diffusion barriers in advanced integrated circuit devices, reflective coatings, and wavelength-selective transparent optical films because of their excellent corrosion and erosion resistance, high hardness, and desirable optical and electrical properties. Polycrystalline TiN films have been prepared by several techniques, including most physical film deposition techniques such as reactive evaporation[1], reactive sputtering[2], dual ion beam deposition[3], ion plating[4], and chemical film deposition techniques such as plasma-enhanced chemical vapor deposition[5]. However, most of these techniques need moderate to high temperatures to

produce crystalline TiN films. At high deposition temperatures the use of TiN films is limited to only some applications where the substrates can withstand elevated temperatures. It is difficult to obtain the high surface mobility required for the nucleation and growth of crystalline films at low substrate temperatures. This limitation can be overcome by delivering the materials to the substrate in highly excited states and/or with appreciable kinetic energy. This is accomplished using PLD. Several researchers have reported the formation of TiN films by PLD using ablation of either Ti targets in nitrogen atmosphere [6,7,8] or stoichiometric TiN targets[9,10,11]. Titanium nitride films deposited by evaporation of Ti targets with CO<sub>2</sub> laser in nitrogen background on stainless steel have been reported to have a hardness of 1900 HV[6]. J. C. S. Kools et al.[8] concluded that it was virtually impossible to grow stoichiometric TiN films by reactive ablation of Ti in a N<sub>2</sub> atmosphere, due to oxygen contamination. Epitaxial growth of TiN films on silicon (100) by KrF excimer laser ( $\lambda=248$  nm,  $\tau=25$  ns) at 600 °C has been reported[9,10]. Titanium nitride films having microhardness of 11.0-17.0 GPa were obtained using XeCl excimer laser deposition ( $\lambda=308$  nm,  $\tau=45$  ns)[11].

Silicon nitride films are important as dielectric materials and functional memory layers in microelectronics and optoelectronic devices. Si<sub>3</sub>N<sub>4</sub> coating is also a potential candidate for use cutting tools, heat engines, and

gas turbines. Due to high thermal stability, chemical inertness, hardness, and low density ( $3190 \text{ kg/m}^3$ ), silicon nitride can be used as protective coatings in high temperature application.

A. Kumar et al. [12] have produced silicon nitride films in nitrogen environment having hardness of 25 GPa at  $700 \text{ }^\circ\text{C}$ . They have also reported the uniqueness of PLD for depositing  $\text{Si}_3\text{N}_4$ : (1) this process provides stoichiometric films, (2) thin film deposition is performed at a relatively low temperature, and (3) laser deposition rate is relatively high. Some researchers have performed ablation of Si wafers in low-pressure ammonia ( $1 \text{ } \mu\text{bar}$ -  $1 \text{ mbar}$ ) to produce  $\text{Si}_3\text{N}_4$  films [13]. In this report the films deposited were a mosaic of different phases such as amorphous silicon nitride, amorphous non-stoichiometric silicon nitride, and amorphous silicon. Non-stoichiometric ( $\text{N/Si} \approx 0.3$ ) and sub-stoichiometric ( $\text{N/Si} \approx 1.0$ ) silicon nitride films by PLD have been reported [14, 15].

The main purposes of this research are to understand the basic mechanism of PLD technique through the deposition of titanium nitride films, silicon nitride films, and composite films consisting of two different nitride films, to maximize the quality of films in which hardness and elastic modulus should be high enough to be hard coatings.

## CHAPTER 2

### LITERATURE REVIEW

#### 2.1 Pulsed Laser Deposition

##### 2.1.1 Principle of Excimer Lasers

Excimer is an acronym for EXCited diMER, a rare gas dimer based on the rare gas halogen. Excimer lasers are high pressure, pulsed gas lasers that give rise to UV light with wide a range of wavelengths from 193 nm to 351 nm.

Energy is pumped by avalanche electric discharge excitation in a gas mixture composing of a rare gas (Ar, Kr, Xe), a halogen gas (F, Cl), and a buffer gas (He, Ne). The pumping generates ionic and electrically excited species that react chemically and produce excimer molecules. Once excimer molecules are formed, they will decay rapidly emitting photons, which are the excimer lasers with wavelengths in the UV range, during the transition from upper electronic state to lower ground electronic state.

The primary reaction channels for KrF excimer laser are shown in Table 2.1[16]. The reactions initiate from electron attachment to the fluorine molecule, followed by ionization of the krypton, excimer formation, and spontaneous and stimulated emission. The absorption reactions including photodissociation and photodetachment occur. Figure 2.1 shows the electronic potential of the KrF excimer laser [17].

Table 2. 1 Primary Reaction Channels for KrF  
Excimer[16]

$F_2 + e \rightarrow F^- + F$	Electron Attachment
$Kr + e \rightarrow Kr^* + e$	2-step ionization
$Kr^* + e \rightarrow Kr^+ + 2e$	
$Kr^+ + F^- + Ne \rightarrow KrF^* + Ne$	3-body Excimer Formation Reaction
$KrF^* \rightarrow Kr + F + hv$	Spontaneous emission
$KrF^* + hv \rightarrow Kr + F + 2hv$	Stimulated emission ( LASER ACTION )
$F + F + Ne \rightarrow F_2 + Ne$	3-body recombination ( very slow )
$F_2 + hv \rightarrow 2F$	Photodissociation
$F^- + hv \rightarrow F + e$	Photodetachment

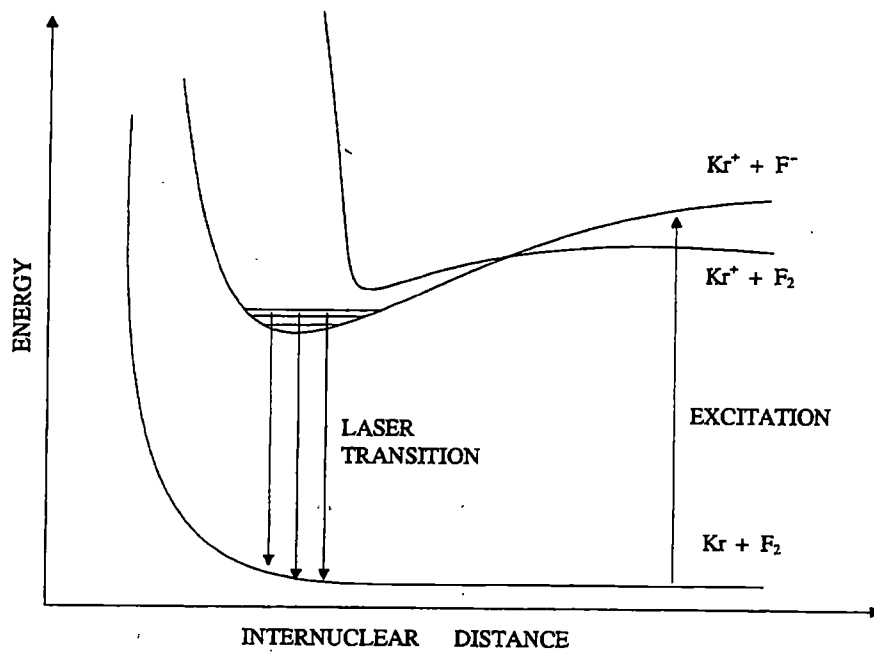


Figure 2. 1 Electronic states in excimer emission[17].



### **2. 1. 2 Basics of PLD**

Figure 2. 2 is a schematic diagram of a pulsed laser deposition apparatus [18]. It has a target holder and substrate holder in a vacuum chamber. Energetic laser beams focused by a set of optical components reach the target through the UV- transmission window. When the laser beam impinges on the target, photons are absorbed by the surface of the target, resulting in the evaporation of target materials. Evaporants produce a plume consisting of a mixture of atoms, molecules, and electrons. Since the collision mean free path in the dense plume is very short, the plume expands rapidly from the target surface forming a nozzle jet with a highly directional flow normal to the target surface. The substrate on which films are to be grown is mounted in the path of the plume. Each laser pulse forms a new plume from the target and deposits new material on the film surface.

### **2. 1. 3 Film Growth Modes**

It is extremely important to understand the film growth mechanisms and pathways that determine the film microstructure, orientation, and properties. Also a good knowledge of the several factors that influence the film growth modes is required in order to be able to adjust the operational parameters to achieve the expected film properties. Greene[19] reviewed the conventional theory of film nucleation and growth based upon the idea that the

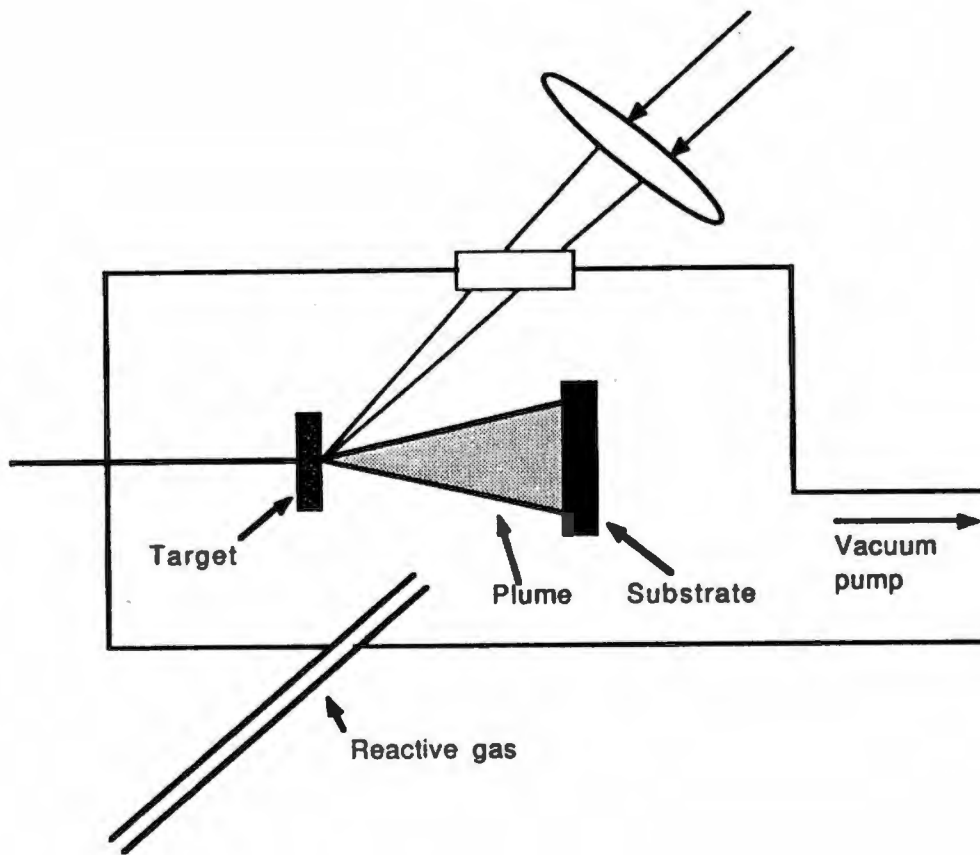
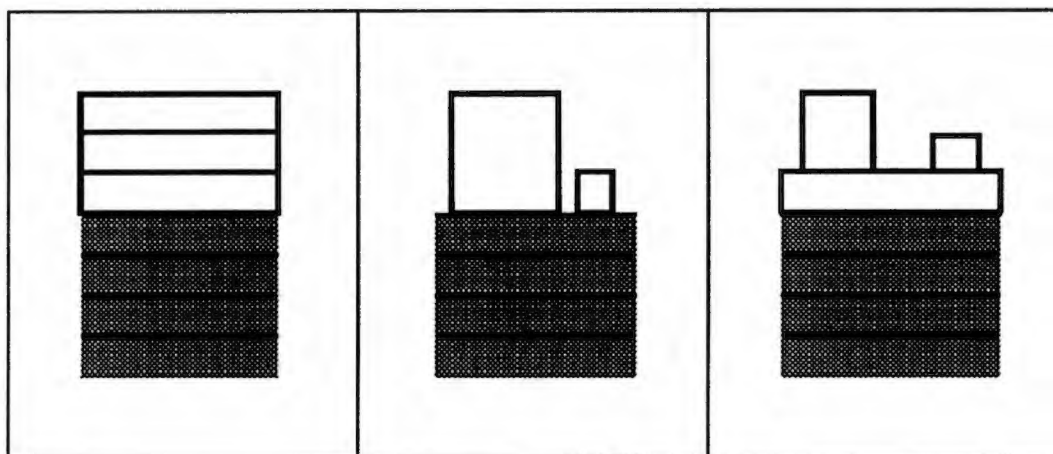


Figure 2.2 Schematic diagram of a PLD apparatus[18].

preference for one of the growth modes depends on the surface free energy of the substrate, the surface free energy of film, and the interfacial free energy between film and substrate. Thermodynamically, all the reactions including nucleation and growth proceed toward the state where the free energy is decreased. Assume the film is in the form of a spherical droplet on the substrate surface. The effect of the substrate surface free energy is to minimize free substrate area by spreading the film droplet out. The effect of the film surface free energy is to minimize free film area by decreasing the radius of the film droplet. The effect of the interfacial free energy between film and substrate is to minimize the contact area by decreasing the radius of the film droplet.

As shown in Figure 2.3, three growth modes have been widely known as major modes for film growth. When the surface free energy of the film and the interfacial free energy between film and substrate are decreased, the contact angle between the droplet and substrate increases forming three dimensional islands. This island growth mode is called the Volmer-Weber mode. When the surface free energy of the substrate is decreased, the contact angle decreases and the film droplet is extended in two dimensions resulting in a monolayer on the substrate. This two dimensional layer growth is called the Frank-van der Merwe mode. The Stranski-Krastanov mode is a combination of the previous two modes. In this mode islands are formed on one or more monolayers of



(a)

(b)

(c)

Figure 2. 3 Film growth modes; (a) Frank-van der Merwe, (b) Volmer-Weber, and (c) Stranski-Krastanov.

the film. The strain energy accumulates in the growing film for the first few monolayers due to film-substrate lattice mismatch. After some film thickness is reached, the film starts to release its strain energy and island formation becomes much more favorable than layer growth. Misfit dislocations and stacking faults are formed to accommodate the new lattice mismatch.

The preceding discussion assumed high surface mobility to allow the free energy to determine the film growth. A decrease in surface mobility can lead island growth to prevail over layer growth and vice versa. Surface mobility can be influenced by the substrate quality, substrate temperature, the arrival rate of atoms on the surface of substrate, and so on.

#### **2. 1. 4 Advantages of PLD**

Recently D. H. Lowndes[20] made a summary of advantages and disadvantages of PLD. If appropriate laser energy density, beam spot size, and shape are selected, stoichiometric transfer of material from target to film can occur in a finite range of deposition angles. The stoichiometric transfer can be achieved only if the laser energy density is high enough to form laser generated plasma. This laser generated plasma causes erosion of target material resulting in the stoichiometric transfer of all of the constituents of a complex and multi-element material.

Since there is no electron beam or hot filaments in the deposition chamber, it is possible to deposit films through reactive deposition in ambient gases. Simple compound films can be obtained by reactive deposition if the proper ambient gas is introduced into the chamber. Also, collisions with ambient gas molecules can be used to control the ablation beam kinetic energy that affects the point defect concentration in the film.

Film growth by PLD is achieved within a laser-generated plasma. A variety of species in the plume possess kinetic and potential energies that can increase sticking coefficients, surface mobilities of adatoms, and nucleation due to high energy chemical reactions. Thus, epitaxial growth of films can be obtained under the proper experimental conditions such as appropriate substrate temperature. Also, growth of multilayered epitaxial heterostructures or superlattices in which each layer can be a chemically complex material is possible provided several chemically complex targets with rapid target exchangers are introduced.

#### **2. 1. 5 Disadvantages of PLD**

There have been two main limitations that impede the development of PLD technique: particulates and the production of an angular distribution of ablated materials. Particulates can be a serious problem for semiconductor films and optical films in which they can produce defects

and scattering centers that decrease carrier mobility, shorten the mobility life time, and degrade the damage threshold of optical films[18]. Production of an angular distribution of ablated material is the barrier to be overcome in order to obtain films of uniform thickness on their substrate.

a) Particulates

Three mechanisms have been reported for particulate formation, according to their phase of origin when they were ejected from the target: solid, liquid, and vapor[21]. Microcracks present in a fresh target or crater edges and columns produced by exposure to continuing laser irradiation are mechanically weak and have a tendency to dislodge from the target due to the laser-generated thermal and mechanical shocks. The size of the particulates produced by these extractions is in the micron and submicron range. The shape of these particulates tends to be spherical when they are melted by laser irradiation otherwise irregular shapes are obtained.

There are two possible mechanisms to explain the particulate formation from the liquid phase. One is by splashing of the molten layer that is generated by superheating of the surface layer. The other is by the laser induced recoil pressure generated by rapid surface evaporation from the molten liquid layer. The particulates

forming from the liquid phase have a few microns in size and a spherical shape.

The condensation from the vapor phase produces very fine particulates, in the range of nanometers. When the pressure of ambient gas is sufficiently high, many collisions with the gas molecules lead to nucleation and growth of fine particulates before they arrive at the substrate. The shape of the particulates forming from the vapor phase is spherical or polygonal.

It has been reported that particulate generation is mainly affected by both the laser parameters and the material properties. The density and size of particulates increase with the laser energy density above the threshold laser energy density for particulate generation. An example of increase in the number density of particulates in YBCO films produced by XeCl laser is shown in Figure 2.4 [22]. A simple way to decrease the number of particulates is to reduce the laser power density below the threshold value for the splashing of the molten layer.

Not only the laser energy density but also the laser wavelength can affect the density and size of particulates. Generally, the density and size of particulates produced by longer laser wavelength are much higher than those produced by shorter laser wavelength. Because photons with short wavelength penetrate less into the target due to absorption, the ejection of molten material occurs only within a very thin layer. A typical example of SEM micrographs of the



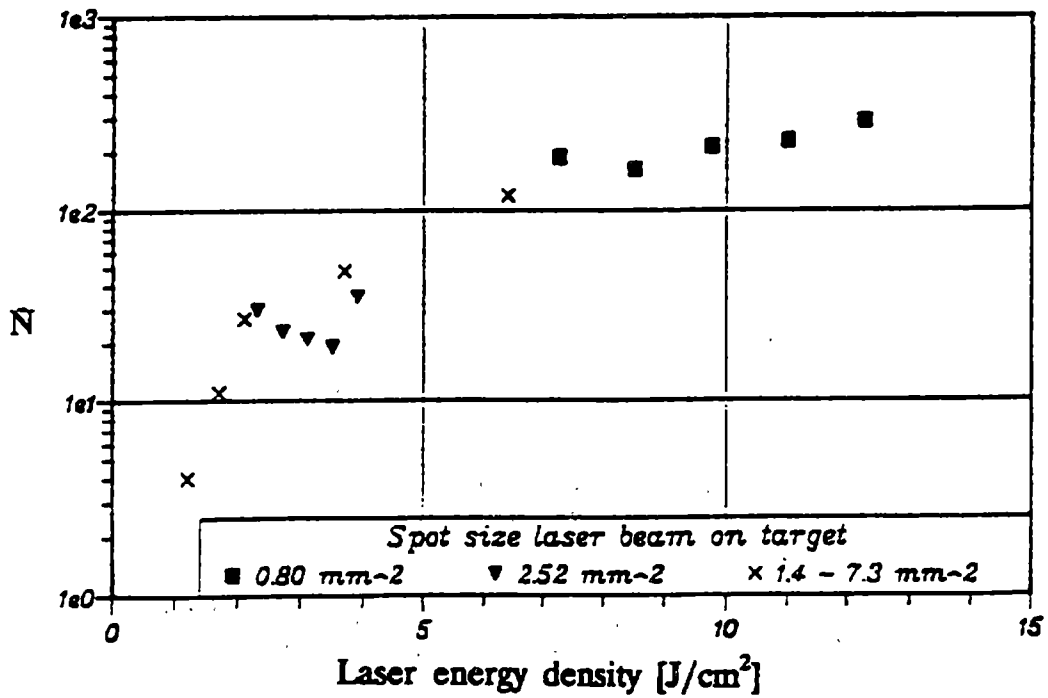


Figure 2. 4 The number of particulates corrected for the film thickness vs. the laser energy density in YBCO films produced by XeCl laser ablation[22].

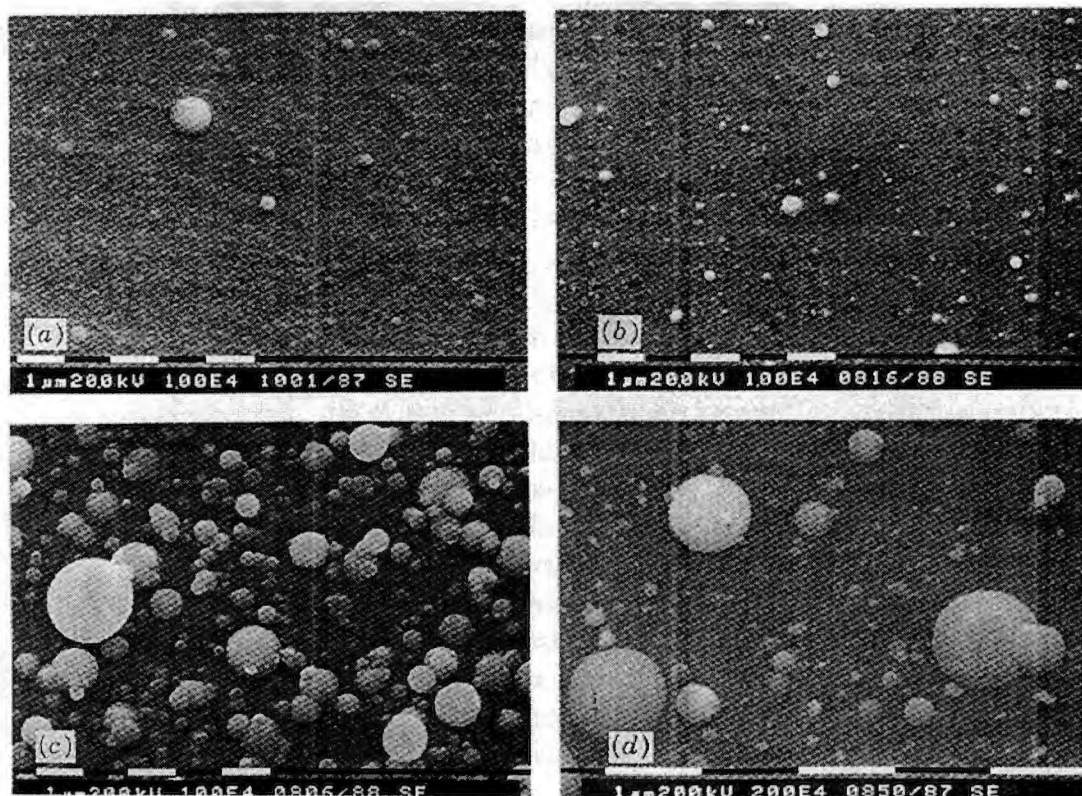


Figure 2. 5 SEM micrographs of PLD thin films with a peak power of  $0.79 \text{ GW/cm}^2$ : (a) 266 nm, 9000 pulses; (b) 355 nm, 9000 pulses; (c) 533 nm, 15,000 pulses; (d) 1064 nm, 15,000 pulses. Scale marker;  $1 \mu\text{m}$ [23].

deposited YBCO at different wavelengths is shown in Figure 2.5[23]. The most effective way to minimize the density and size of particulates is to use short wavelength such as KrF (248 nm) or ArF (193 nm) excimer lasers.

The size of very fine particulates produced by condensation from the vapor species is affected by the ambient gas pressure. The size of particulates increases with increasing ambient gas pressure because increased frequency of collisions between the vapor species and ambient gas molecules leads to the nucleation and growth of fine particulates before they reach the substrate. Figure 2.6 shows the cumulative size distribution of fine particulates as a function of ambient gas pressure[24]. The increase in size and broader size distribution were obtained at higher ambient gas pressure. Since the growth of fine particulates occurs by diffusion, the longer the residence time in vapor the larger the particulate. Thus, the particulates formed at a long distance between substrate and target are larger than those forming from at a short distance.

The properties of the target can also affect characteristics of particulates. A low-density target produces large irregular shaped particulates resulting from the fragments due to the weak bonding while a high-density target generates spherical shaped particulates by splashing[25]. As mentioned previously, a rough target surface gives rise to large particulate sizes. Therefore,

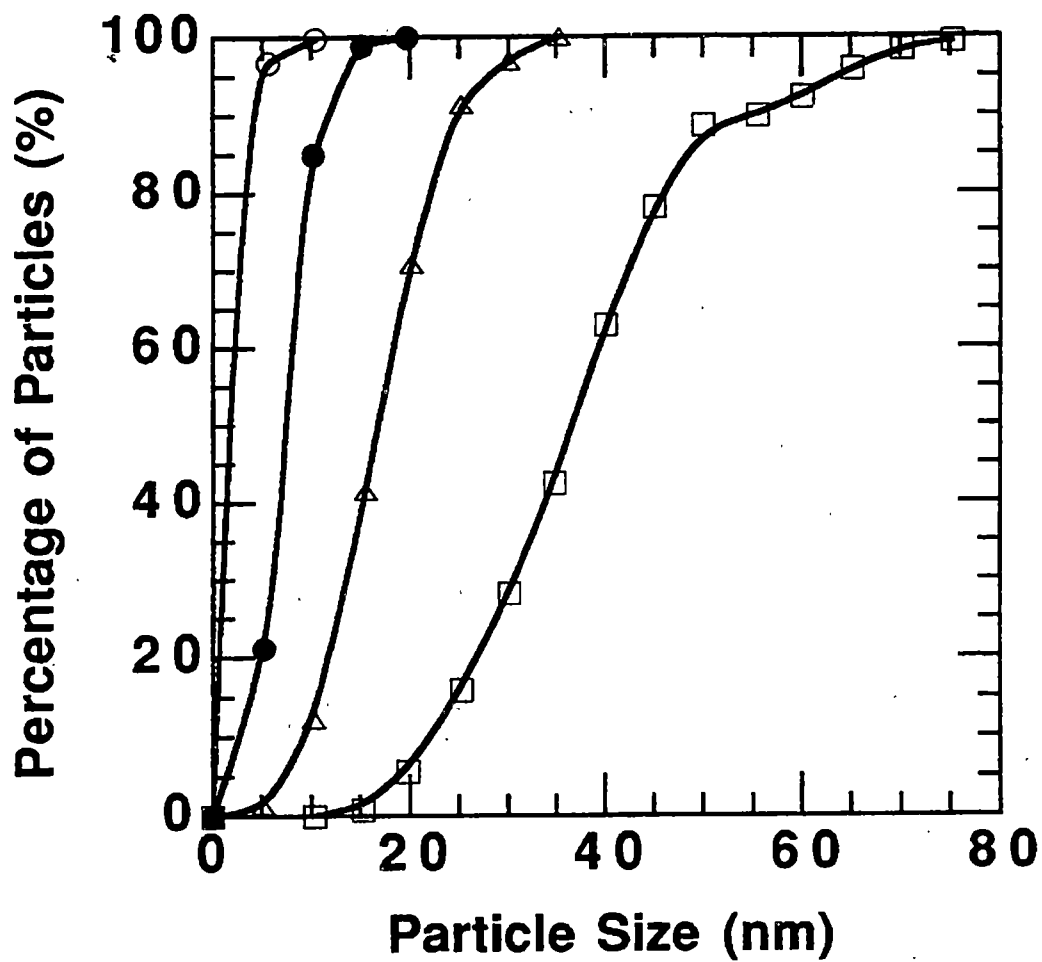


Figure 2. 6 Cumulative size distribution of ultrafine Fe particulates made under Ar pressure of 0.1, 1.3, 13.3, & 200 kPa [24].

selection of a high-density target with smooth surface and target resurfacing after laser irradiation are required to minimize the presence of particulates. There are other methods to counter the presence particulates, e.g., velocity filter, dual-laser, and off-axis ablation.

#### b) Angular Distribution

The other disadvantage of PLD is production of an angular distribution of ablated materials. Methods of measurement, experimental observation, and modeling related to angular distribution have been reviewed by Saenger[26]. The source angular distribution  $f(\theta)$  and the film thickness distribution  $D(\theta)$  are thought to exchange each other in PLD consideration.  $\theta$  is the angle between the radial vector and target normal. For the case of deposited film on a flat substrate parallel to the target, the source distribution  $f(\theta) = (\cos\theta)^p$  would generate a film thickness distribution  $D(\theta) = (\cos\theta)^{p+3}$  [26]. Two methods have been used to measure angular distribution from PLD: Film based method and Probe based method. In the film based method, the angular distribution  $D(\theta)$  is simply measured by measuring the thickness of the film at each distance  $x$  from the ablation center axis and  $\theta = \tan^{-1}(x/h)$  in Figure 2.7. However, this method is based on the assumptions that the ablated particles have a unity-sticking coefficient and the depositing film is not resputtered by the incident flux of particles. The probe based method measures the source

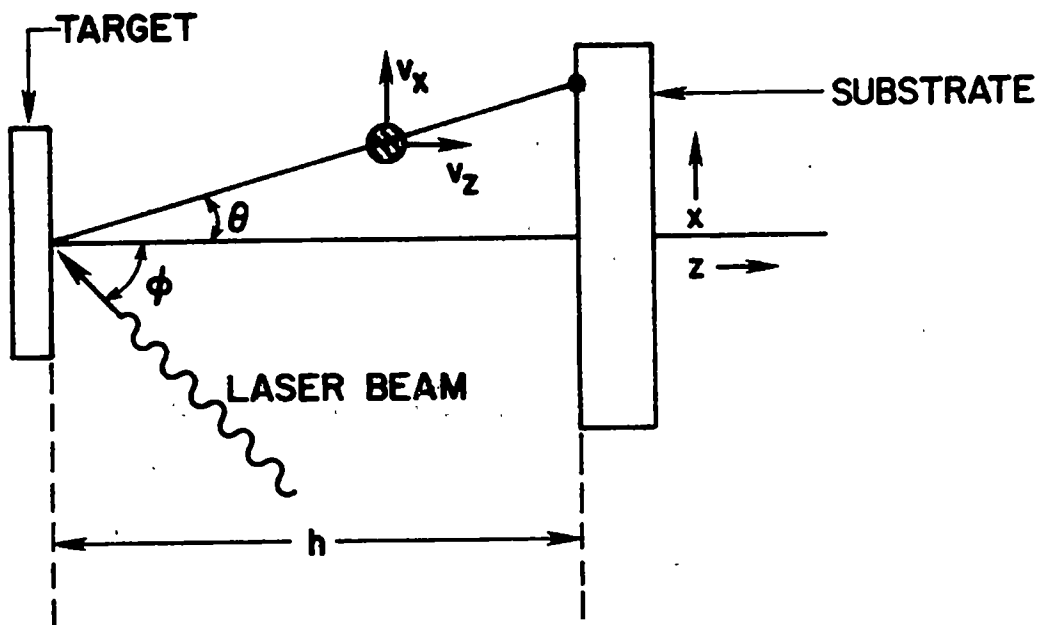


Figure 2. 7 Deposition geometry[26].

angular distribution with an ion probe or mass sensitive detector in which probe or detector measures the flux emitted from the target into different angles.

The angular distribution can be affected by various experimental parameters such as laser parameters, system geometry, target properties, and ambient gas. Although research on the effect of duration time, laser energy density, and wavelength on the plume distribution have been widely done, only few results were established. For the effect of focused spot size on the angular distribution, there is a clear nonequivalence between a single spot and a small spot scanned over the same area; the latter providing a much broader than the former. This effect stems from the fact that forward peaking increases with the number of intraplume collisions per particle.

The angular distribution is expected to remain constant with target-substrate distance when no collisions among particles occur in vacuum. However, change in the source distribution with target-substrate distance has been observed for carbon[27] in which a broader angular distribution was obtained at shorter distances. This phenomenon is thought to result from scattering of the incident flux with particles resputtered and reflected from the substrate. When an ambient gas is introduced, the plume angular distribution becomes broader since particles in the plume undergo collisions with the background gas resulting

in the scattering of particles away from their original trajectories.

More detailed measurements incorporate the variation in composition of film by PLD with angle from the center axis even though PLD has been known as a method that produces the same film composition (stoichiometry). If two assumptions (unity sticking coefficient and no resputtering) for the film based method are valid, the variation in film composition means that different chemical species in the plume have different angular distributions. The different angular distributions of different species in the plume may be caused by discrepancy of the charge of species and their mass. Also the sputtering by background gas can be one of the reasons that causes the variation in composition of film with angle.

## **2.2 Hard Coatings**

### **2.2.1 Hard Materials for Coating**

It is impossible to select a material that satisfies many desired properties such as high hardness, toughness, and good adherence at the same time for hard coating applications. Figure 2.8 shows a diagram of the factors that affect the properties of coating materials[28]. Three factors can be pointed out: constitution, fabrication parameters, and microstructure. Constitution of substrate and film as well as fabrication parameters such as coating



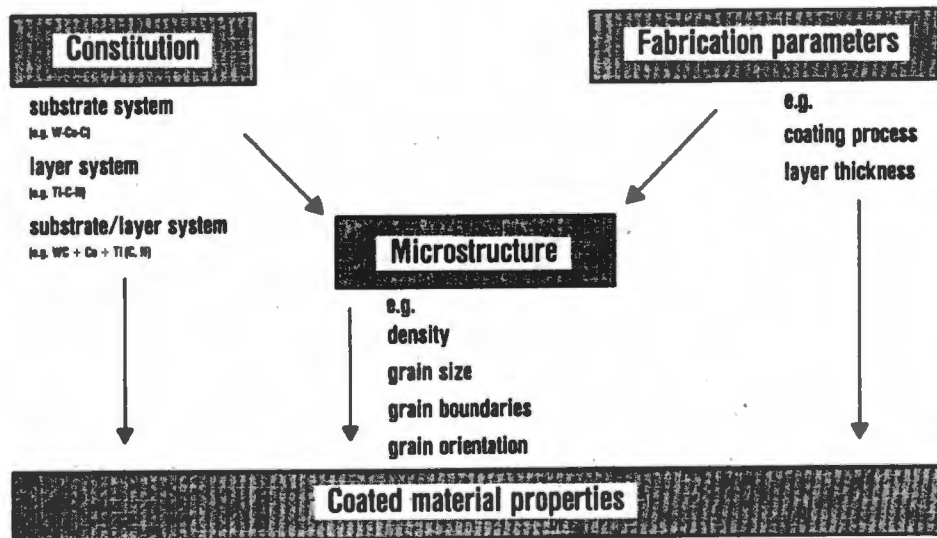


Figure 2. 8 Factors affecting coated materials properties[28].

thickness and deposition methods determine the microstructure of the coating. The required properties of the hard coatings can be obtained by an appropriate combination of these three factors.

Hard materials for coatings were divided into three groups as determined by their chemical bonding[28]: metallic hard materials(borides, carbides, nitrides of the transition metals), covalent hard materials(borides, carbides, nitrides of Al, Si, B, and diamond) and ionic hard materials. Table 2.2 shows the properties of these three groups of hard materials. From Table 2.2, some general facts can be deduced as described in the following: Every hard material of the three different groups has both advantages and disadvantages in its application for hard coating. The transition metal borides/carbides/nitrides seem to be most adequate hard coating materials. However, owing to the multiple demands such as high hardness, high toughness, stability, and good adherence at the interface, multilayer coatings or multiphase coatings were proposed to meet these complex requirements. The most important feature in developing multilayer coatings is to obtain sufficient adherence at the interface between layers. For multiphase coatings, the phases with coherency at the interface should be chosen to get sufficient bonding between layers. It has been reported that nano-dispersed TiC/ TiB<sub>2</sub> layers with coherency at the interfaces were obtained with up to 5  $\mu\text{m}$  coating by successive sputtering from a TiC and TiB<sub>2</sub> cathode

Table 2. 2 Properties of Hard Materials[28]

Group	Material	Melting Point (°C)	Hardness (HV)	Elastic Modulus (kN/mm <sup>2</sup> )	Density (g/cm <sup>3</sup> )
Metallic Hard Materials	TiB <sub>2</sub>	3225	3000	560	4.50
	VC	2648	2900	430	5.41
	TiC	3076	2800	470	4.93
	ZrC	3445	2560	400	6.63
	WC	2776	2350	720	15.72
	TiN	2950	2100	590	5.40
	ZrN	2982	1600	510	7.32
	TaC	3985	1550	560	14.48
Covalent Hard Materials	C	3800	~8000	910	3.52
	SiC	2760	2600	480	3.22
	Si <sub>3</sub> N <sub>4</sub>	1900	1720	210	3.19
	AlN	2250	1230	350	3.26
Ionic Hard Materials	Al <sub>2</sub> O <sub>3</sub>	2047	2100	400	3.98
	BeO	2550	1500	390	3.03
	ZrO <sub>2</sub>	2677	1200	190	5.76
	TiO <sub>2</sub>	1867	1100	205	4.25

or by simultaneous sputtering from a TiC/TiB<sub>2</sub> cathode [29]. These layers have exhibited better wear resistance than single-phase layers primarily by virtue of better adherence and high toughness.

### 2.2.2 Hardening Mechanisms in Coatings

The strength of materials is determined by the formation and movement of dislocations and formation and propagation of cracks. The stress required for the formation and motion of dislocations depends on the elastic modulus of the material[30]. It has been realized that an alloy with a smaller grain size has a higher strength. This is well understood in terms of the Hall-Petch model. The dislocations move and a new dislocation will be generated if there is sufficient applied stress that is larger than a critical stress. This process will cease when the stress field produced by the multiplication of the dislocations offsets the applied stress. The simple relationship between the critical stress and grain size was derived as

$$\sigma_c = \sigma_0 + kl^{-1/2}$$

This Hall-Petch relation is valid only for sufficiently large grains that can accommodate the dislocation source (about  $\geq 100$  nm). Therefore, it can not explain the enhanced strength of nanometer-sized structures.

Koehler[31] suggested that a high-strength material could be obtained by fabricating a structure consisting of a few nanometer thin layers of two materials A and B with a high and low elastic modulus. The Frank-Read source for dislocation multiplication can not be produced in such thin layers. He also mentioned that the interfaces between layers would act as an obstacle, preventing dislocations from moving. Atoms around a dislocation are displaced from their regular lattice sites, having strain energy that is proportional to the modulus of the materials. Thus, the strain energy increases when a dislocation moves into a layer with higher modulus. The dislocations will be formed only in material B with lower modulus. There is a repulsive force that increases as dislocations in a layer with lower modulus  $G_B$  approach the interface with the layers with higher modulus  $G_A$ . According to Koehler's model, the critical stress required to move a dislocation across the interface is proportional to a certain value of  $(G_A - G_B)/(G_A + G_B)$ . A structure having a large difference in modulus between two layers requires a large critical stress to move a dislocation. In other words, this structure has a high hardness since the hardness of a material can be represented as  $H \approx 3\sigma_c$ [32]. There have been reports of large hardness enhancement, up to 50 GPa for TiN/VN and TiN/NbN with a large difference in shear modulus between two layers[33,34]. However, for the epitaxial heterostructures of TiN/VN and TiN/NbN films, a maximum of the hardness at

about 5 and 8 nm of superlattice period (thickness of the combined two layers) can not be explained by Koehler's model alone. The variation of the hardness as a function of the superlattice period is shown in Figure 2. 9[35].

A further insight into the hardness enhancement mechanism in the nitride superlattice coating was proposed[35]. When the superlattice period( $\Lambda$ ) is very small (1~2 nm), the layers become almost interdiffused so that the modulus of each layer becomes close to each other. Also, for very small values of  $\Lambda$ , opposing forces can be exerted on dislocations at an interface, which decreases the stress necessary to move the dislocations. The overall impact of these two effects is that the hardening effect of the interface is reduced when the layers are narrow and the superlattice shows no hardness enhancement. The stress needed to bend a dislocation to a radius  $R$  in a material of shear modulus  $G$  is proportional to  $G/R$ . But  $R$  is proportional to layer thickness, which in turn is proportional to  $\Lambda$ . The minimum stress for this type of dislocation motion is approximately proportional to  $G/\Lambda$ . In other words, the hardness of a superlattice decreases as  $\Lambda$  increases. The maximum hardness at intermediate values of  $\Lambda$  occurs when the stresses required to move dislocations by the two mechanisms become equal.

Dislocation motion is inhibited by coherency stresses. These stresses arise in superlattices when the layer materials have different lattice constants. Since the

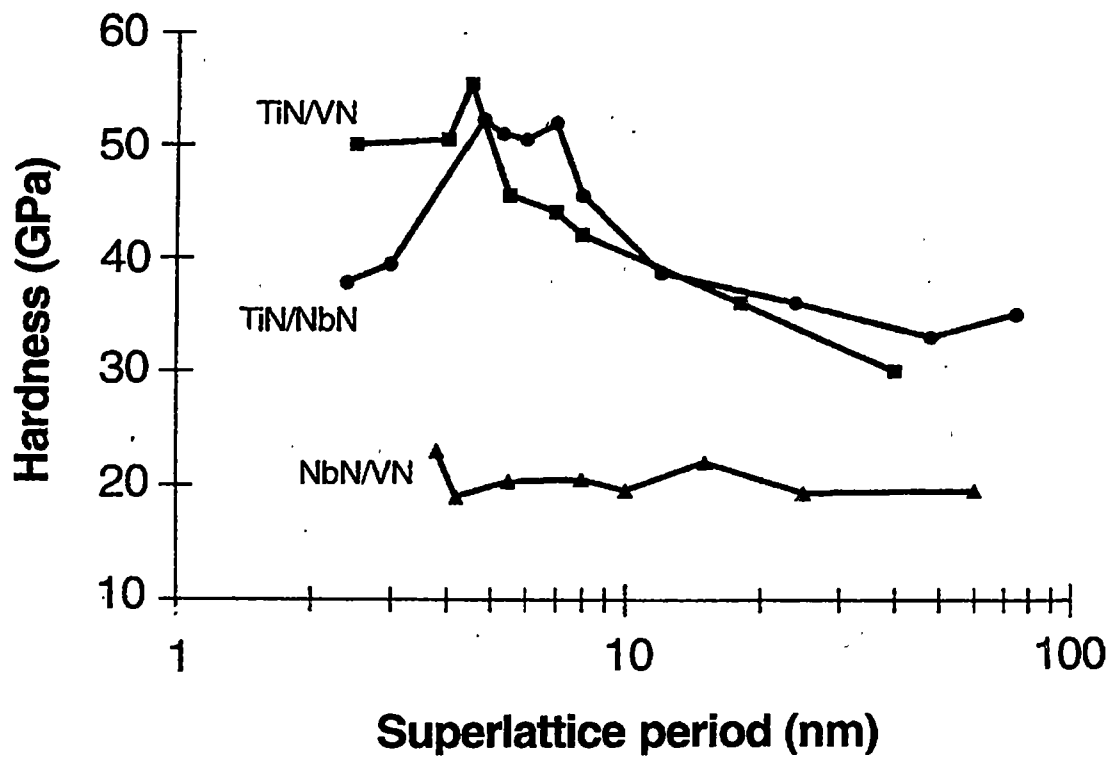


Figure 2. 9 Hardness of polycrystalline superlattice films of TiN/NbN, TiN/VN, and NbN/VN as a function of the superlattice period[35].

lattice planes actually match across the layers, the difference in the lattice parameters must be relieved by elastic strain in the layers themselves. These strains exert forces on the dislocations, making it more difficult for them to move across an interface. Thus, increase in hardness of the materials ensues. However, this effect is restricted to small values of  $\Lambda$  because the strains are relaxed at larger layer thickness by the introduction of interfacial misfit dislocations. It has been reported that the effect of coherency strains is small compared to the effect of difference in shear moduli [36].

### **2. 2. 3 Nanocrystalline Transition Metal Nitrides/ Amorphous $\text{Si}_3\text{N}_4$ Composite Materials.**

Koehler[31] also suggested that hardness enhancement by fabricating alternatively layered structure with two different materials would also occur if one of the materials is amorphous. A few defined features for hard coatings were indicated as follows[37,38]: Interdiffusion, which causes the decrease in hardness, can be avoided by using low-temperature deposition methods. The problems caused by lattice misfit between two polycrystalline materials with randomly oriented grains can be solved once an amorphous material is selected. The grain size of the crystalline component should be nanometer range, that is, close to the stability limit of the crystalline phase. Hardness



enhancement in this composite material is expected because dislocations that might form in the crystalline component can not move through the thin amorphous phase. This new approach to hard materials has been verified by several systems consisting of nanocrystalline transition metal nitride/amorphous  $\text{Si}_3\text{N}_4$  composites (nc- $\text{Me}_x\text{N}/\text{a-Si}_3\text{N}_4$ , Me = Ti, W, V) all of which reached or even exceed the hardness of 50 GPa as the crystal size of nc- $\text{Me}_x\text{N}$  decreases to 3~3.5 nm[39,40].

The basic concepts for hard composite materials can be found from the following rules[41,42]. The composite has to be combined with small nanocrystals( $\leq 4\sim 5$  nm) and thin amorphous matrix(0.3~0.6 nm); the Frank-Read source for dislocation multiplication can not operate in nanocrystals whose diameters are less than 10 nm. Such nanocrystals are free of dislocations. If a dislocation would form in the nanocrystal under huge applied stress, it could not move across the thin amorphous matrix but create a nanocrack in the interface. The conceptual microstructure in Figure 2.10[38] shows that propagation of the nanocrack is hampered.

There are several reasons why the combination of a transition metal nitride and  $\text{Si}_3\text{N}_4$  is the most promising hard coating type. Many transition metal nitrides are strong and crystallize easily even at relatively low temperatures.  $\text{Si}_3\text{N}_4$  is also a strong amorphous solid with a dense atomic network below 1000°C and has a flexibility to relax stresses

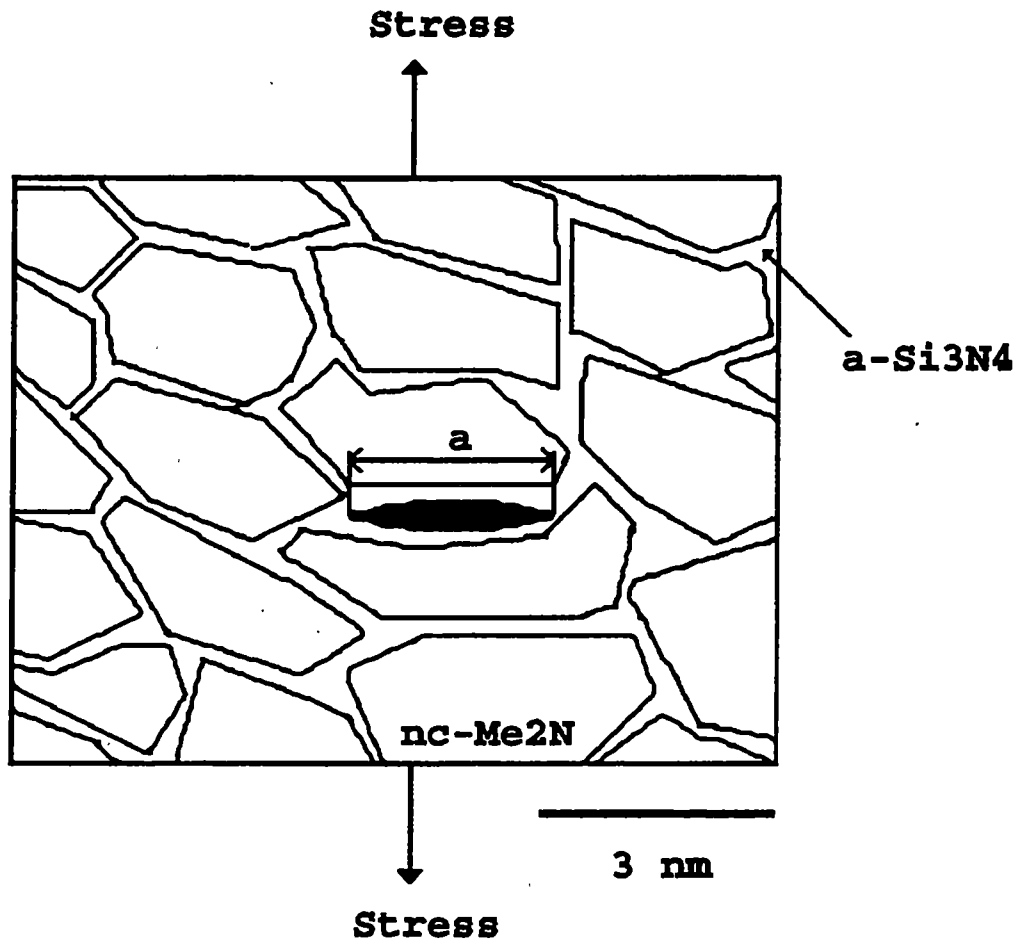


Figure 2. 10 Suggested microstructure of the superhard nanocrystalline composite showing the propagation of nanocracks, which may form under applied stress, is hindered[38].

at the  $nc-Me_xN/a-Si_3N_4$  owing to the combination of the fourfold coordination of Si and threefold coordination of N. For both cases,  $TiN/Si_3N_4$  and  $W_2N/Si_3N_4$  prepared by plasma chemical vapor deposition at  $500\sim 550^\circ C$  [39,40], the hardness and elastic modulus increase with increasing silicon content and reach a maximum value of  $3.0\sim 3.5$  nm. Maximum hardness and elastic modulus are  $5000\text{ kg/mm}^2$  and  $50\text{ GPa}$ , respectively. The hardness and elastic modulus decrease and the crystallite size increases as the content of silicon is increased above this threshold value.

## **2. 3 Mechanical Properties of Hard Coatings**

### **2. 3. 1 Hardness and Elastic Modulus**

Hardness implies resistance to plastic deformation by indenters with a variety of geometries such as cone, spheres, flat cylindrical shape and so on. The main purpose of using the indentation technique is to measure the elastic modulus and the hardness that have been known as two necessary parameters regarding the mechanical property of materials.

In the load and displacement sensing indentation methods, a reduced modulus  $E_r$  has been introduced as Equation 2. 1 to account for the contribution of indenters on the load-displacements measurements [43].

$$\frac{1}{E_r} = \frac{(1-\nu^2)}{E} + \frac{(1-\nu_i^2)}{E_i} \dots\dots\dots(2.1)$$

where E and  $\nu$  are Young's modulus and Poisson's ratio for the sample, respectively. The  $E_i$  and  $\nu_i$  are the same values for the indenter. The data from indentation load-displacement were analyzed according to Equation 2. 2 to measure the elastic modulus[44].

$$S = \frac{dP}{dh} = \frac{2}{\sqrt{\pi}} E_r \sqrt{A} \dots\dots\dots(2.2)$$

where S is the experimentally determined stiffness of the upper part of unloading data and A is the contact area. Thus, the elastic modulus can be determined by measuring initial unloading stiffness and area of the hardness impression.

Since the load and depth sensing indentation technique was known to be useful for measuring the mechanical properties of thin films, but the direct imaging of very small hardness impression is time-consuming and difficult, new method measuring contact areas have been proposed. A simple method using load-displacement curve and indenter shape function has been proposed to measure the contact areas[45]. The indenter shape function is the cross-section area of the indenter that varies with the depth of the contact. The contact areas can be estimated from the shape function provided the depth of the contact can be derived from the load-displacement data.

Figure 2. 11 is a schematic diagram of a cross-section of an indentation showing the contact area[46]. The total displacement( $h$ ) is defined as

$$h = h_c + h_s \dots \dots \dots (2.3)$$

where  $h_c$  is the contact depth and  $h_s$  is the displacement of the surface at the perimeter of the contact.  $h_f$  is the final depth after the applied load is completely removed. Oliver & Pharr[46] have assumed that the indenter shape can be illustrated by an area function  $F(h)$  that gives rise to the contact area at peak load.

$$A = F(h_c) \dots \dots \dots (2.4)$$

The function ( $F$ ) should be determined by experiment. From Equation 2. 3, the contact depth is defined as

$$h_c = h_{max} - h_s \dots \dots \dots (2.5)$$

where  $h_{max}$  can be determined by experiment and  $h_s$  is given by Sneddon[47] for a conical indentation as

$$h_s = \epsilon (P_{max}/S) \dots \dots \dots (2.6)$$

where  $\epsilon$  is a geometry constant. The values of  $\epsilon$  for the different indenters vary. For example,  $\epsilon$  is unit for the

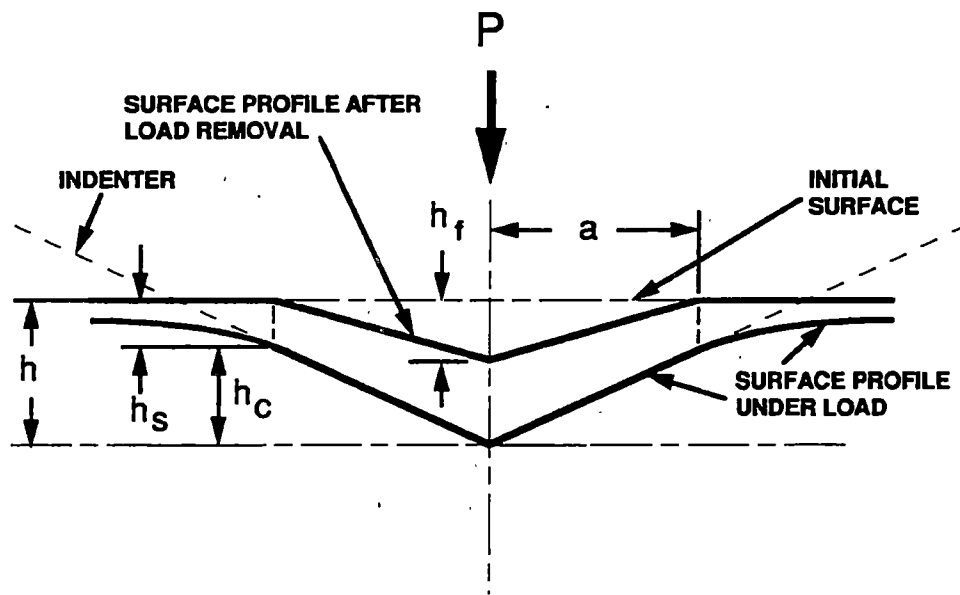


Figure 2. 11 A schematic diagram of a cross-section through an indentation [46].

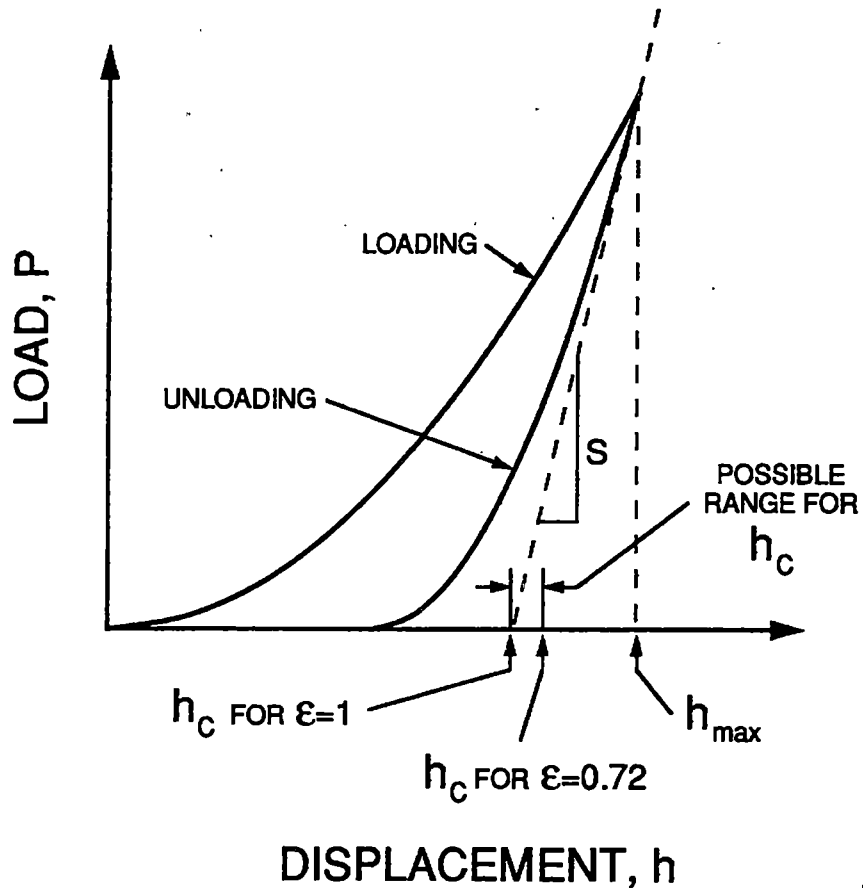


Figure 2. 12 A schematic diagram of load vs. displacement showing the contact depth[46].

flat punch and 0.72 for the conical indenter. As shown in Figure 2. 12, the value of  $h_c$  varies in the possible range for the indenters. The area function for a Berkovich indenter has been established by Oliver & Pharr[46].

$$A(h_c) = 24.5h_c^2 + C_1h_c^1 + C_2h_c^{1/2} + \dots + C_8h_c^{1/128} \dots\dots\dots(2.7)$$

where  $C_n$  are constants. Thus, the elastic modulus( $E$ ) can be calculated by stiffness from the unloading curve and contact area using the area function derived for a Berkovich indenter.

$$E_r = \frac{\sqrt{\pi}}{2} \frac{S}{\sqrt{A}} \dots\dots\dots(2.8)$$

Also, the hardness can be calculated from its conventional definition provided the contact area is known.

$$H = \frac{P_{max}}{A} \dots\dots\dots(2.9)$$

### 2. 3. 2 Internal Stresses of the Coatings

Thin films or coatings can be stressed even without applied external force or load. This stress is called internal or residual stress. Internal stress is not limited to film-substrate structure, but is also found in all kinds of materials under particular environment. A model of the development of internal stresses during film deposition is



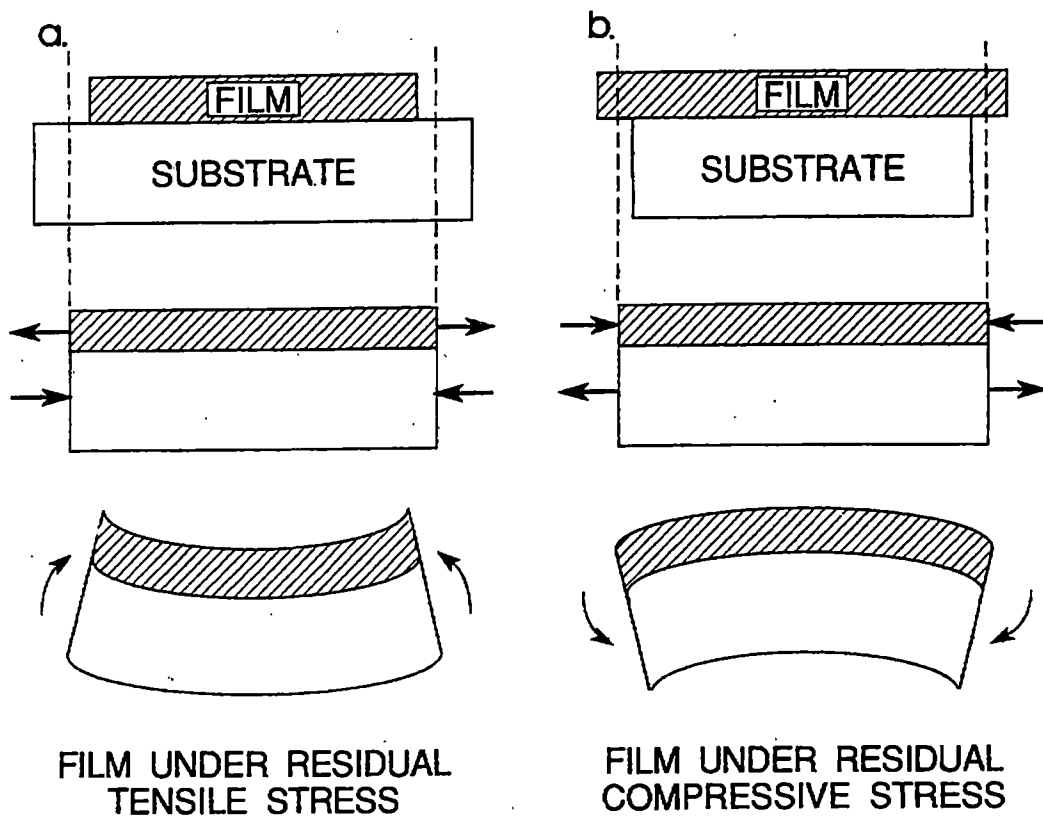


Figure 2. 13 Sequence of events leading to (a) residual tensile stress in film, (b) residual compressive stress in film [48].

shown in Figure 2. 13[48]. As shown in Figure 2. 13. a, the growing film shrinks with respect to the substrate. It has been thought that surface tension and misfit between film and substrate might cause this constriction. In order to achieve the mechanical equilibrium between film and substrate, the film tends to extend and the substrate contracts. The tensile forces in the film are balanced by the compressive forces in the substrate. However, when this combination is not at mechanical equilibrium the film-substrate will elastically bend to compensate for the unbalanced moments. Thus, films having tensile stresses bend the substrate concavely upward as shown in Figure 2. 13. (a) Correspondingly, internal compressive stresses in films bend the substrate convexly downward as shown in Figure 2. 13. (b) Sometimes sufficiently high tensile stress in films results in the film fracture whereas high compressive stress in films causes the wrinkling and loss of local films.

## CHAPTER 3

### EXPERIMENTAL PROCEDURE

#### 3. 1 Materials Used

The substrate used in this experiment was phosphorus-doped silicon(100) wafer provided by Transition Technology, Inc. The thickness of silicon wafer ranged from 475 to 525  $\mu\text{m}$  and resistivity was in the range of 1.0~6.2  $\Omega$  cm.

The targets used were TiN and  $\text{Si}_3\text{N}_4$  with purity of 99.5% and 99.9%, respectively. Both targets provided by Target Materials, Inc. had impurities such as carbon and oxygen. The diameter and thickness of both disc targets were 1" and 0.25", respectively.

#### 3.2 Deposition Process

A Lambda physik LPX-300 excimer laser in the Laser Processing Laboratory at the University of Tennessee has been used to deposit films in this experiment. The pulsed 248 nm UV radiation generated by KrF excimer laser was refracted by two mirrors and focused by two cylindrical lenses and one spherical lens onto the target mounted in the stainless chamber. A base pressure ranging from  $8 \times 10^{-8}$  to  $2 \times 10^{-7}$  torr was obtained with the help of a turbomolecular pump. Both substrate and target were rotated at a rate

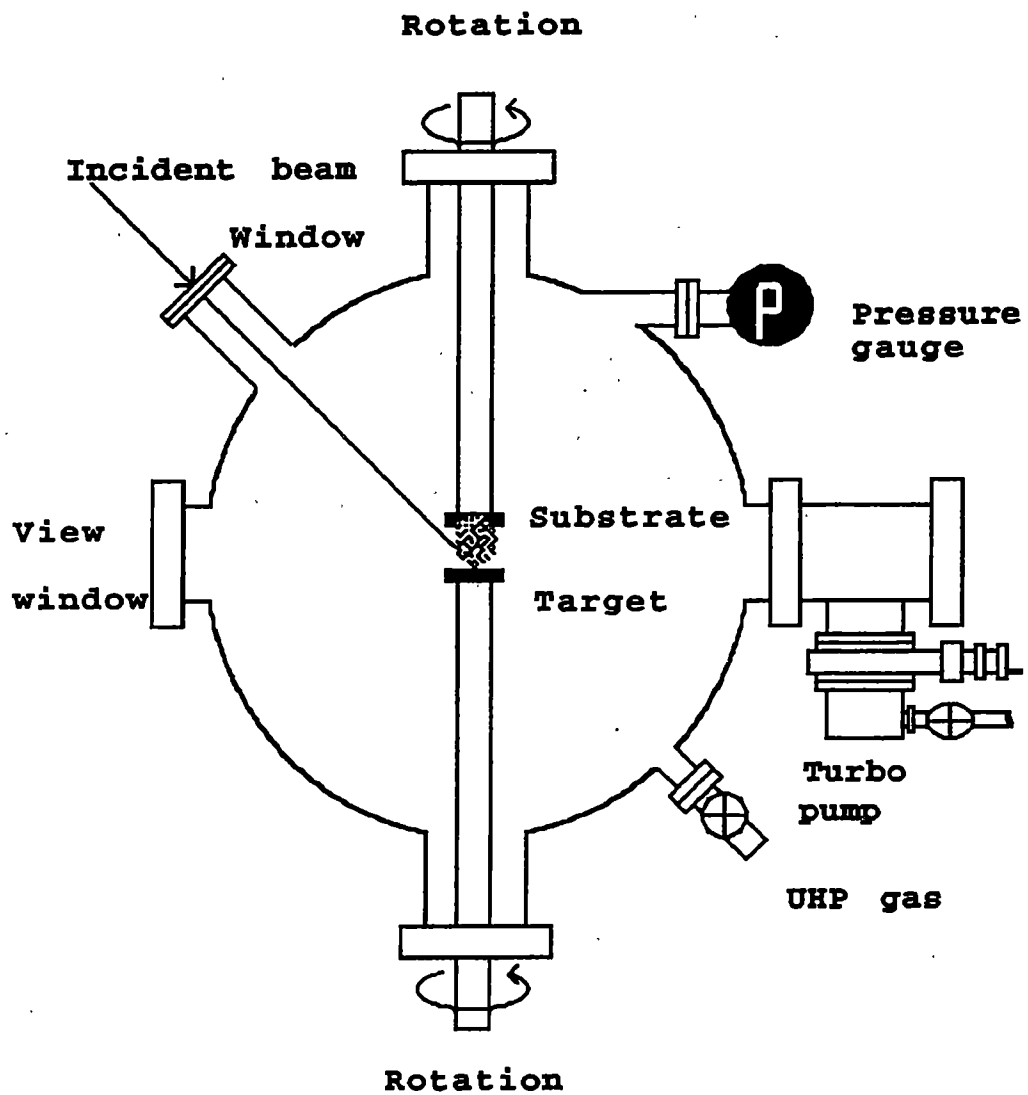


Figure 3. 1 A Schematic diagram of PLD apparatus at the Laser Processing Laboratory, UT.

of 20 ~ 30 rpm to produce uniform films and avoid damaging the targets (Figure 3.1). The pulse repetition rate was varied from 10 to 30 Hz and the distance between substrate and target was varied between 2 and 6 cm. The laser energy density of laser was in the range of 1 ~ 3 J/cm<sup>2</sup>. Before being mounted, all Si substrates were ultrasonically cleaned in methanol for 5 minutes, followed by a dip for 1 minute in 5% HF aqueous solution, and then dried. Deposition rates were determined by measuring the thickness of films as function of numbers of pulses using a Dektak II profilometer.

The films for indentation were deposited at  $E_d = 2.5$  J/cm<sup>2</sup> at 20 Hz and a target-substrate distance of 4 cm. The deposition process were performed in vacuum ( $1 \sim 2 \times 10^{-7}$  torr) at room temperature and in nitrogen atmosphere ( $1 \sim 2 \times 10^{-3}$  torr) at 500 °C. The total thickness of each film was about 500 nm. Four specimens in both conditions were prepared as follows: TiN film (500 nm), Si<sub>3</sub>N<sub>4</sub> film (500 nm), Multi-layered film (layers consisting of TiN 10 nm + Si<sub>3</sub>N<sub>4</sub> 3 nm), Multi-layered film (layers consisting of TiN 10 nm + Si<sub>3</sub>N<sub>4</sub> 1 nm).

### **3. 3 Analysis of Coatings**

#### **3. 3. 1 X-ray Diffraction**

X-ray diffraction has been used to analyze the crystal structure and orientation of films deposited by PLD. In order to increase the X-ray signal coming from the film, the film-thickness was over 1  $\mu\text{m}$ . The X-ray diffractometer used in this research was a Rigaku-Denki diffractometer with a computer controller that could adjust all parameters such as scan rate, step size. X-ray diffraction data were obtained at 30kV and 35 mA using  $\text{CuK}\alpha_1$  ( $\lambda = 0.1542 \text{ nm}$ ) radiation in  $2\theta/\theta$  mode. Diffraction patterns for the TiN and  $\text{Si}_3\text{N}_4$  targets were obtained and compared with the diffraction patterns from the films.

#### **3. 3. 2 Transmission Electron Microscopy**

The crystal structure and orientation of the titanium nitride and silicon nitride films were investigated by TEM. Thin films (40 nm ~ 60 nm) were deposited onto cleaved KBr substrates. After deposition, the KBr substrate was dissolved in distilled water, the film was collected on a slotted 400 mesh copper grid and dried in air. All the films were analyzed either immediately after deposition or after being stored in a desiccator for a few days. A Hitachi H800

TEM operated at 100 kV ( $\lambda = 0.0037$  nm) was used to examine the films. Also Energy Dispersive X-ray (EDX) data were obtained to determine the constituent elements in the films at 100 keV.

### **3. 3 .3 Scanning Electron Microscopy**

The morphology of the films and targets was investigated by SEM. The presence of particulates, a common artifact in PLD, was carefully determined in silicon nitride films. For these measurements the JOEL-840 SEM was operated at 10 kV with a working distance between 15 mm and 48 mm. Also a Cambridge Stereoscan 360 SEM operated at 15 kV was used to examine the surface morphology before (after polishing), and after ablation in both titanium nitride and silicon nitride targets.

### **3. 3. 4 X-ray Photoelectron Spectroscopy (XPS)**

Photoelectron spectra for polished and ablated targets, and films deposited by PLD were obtained using a Perkin-Elmer 500 ESCA at the Chemistry Department. X-ray source was monochromatized Mg  $K_{\alpha}$ ;  $h\nu = 1253.6$  eV, operated at 15 kV and 20 mA. The base pressure in the XPS chamber was  $\sim 6 * 10^{-9}$  torr. Prior to the analysis the specimens were sputtered for 5 minutes using a Perkin-Elmer 300 argon ion gun operated at

3 keV. Survey scans were performed with an analyzer pass energy of 178 eV over and a binding energy range from 0 to 1000 eV.

The binding energy scale was calibrated using as a reference binding energy of Au  $4p_{7/2}$  peak at 84.0 eV. The correction to the binding energy shift due to surface charging was determined by measuring the Ar  $2p_{3/2}$  peak of implanted Ar<sup>+</sup> ions. The reference position of this peak was 242.2 eV.

The relative atomic concentration of each element in the specimens was determined adopting reference sensitivity factors of the silicon nitride and titanium nitride targets used in this experiment.

### **3. 3. 5 Nanoindentation**

All experiment to measure hardness and elastic modulus of films were carried out using a Nanoindenter®II (Nano Instrument, Inc., Knoxville, TN) located in the Metals and Ceramics Division at the Oak Ridge National Laboratory. A schematic of the instrument is shown in Figure 3. 2. The system uses a three-side pyramid Berkovich indenter. The indenter's position is determined by a capacitive



displacement sensor with a resolution of 0.16 nm. The indentation column is supported by a spring, and the force on the column is controlled by varying the current in the coil. The load resolution is 0.3  $\mu\text{N}$ .

The test involves driving the indenter toward the surface of the test sample at a constant rate, detecting the surface as a change in velocity. After the surface has been detected, the indenter is forced into the specimen at a different but still constant rate. The system continuously records the displacement and forces associated with indentation process for a pre-set sequence (load to a certain depth, unload a specified amount, reload to deeper depth, hold for a certain time, unload totally). Twelve segments were used in this study as summarized in Table 3.

1. Fifteen data for each specimen were obtained and averaged excluding data that were completely deviated from others.

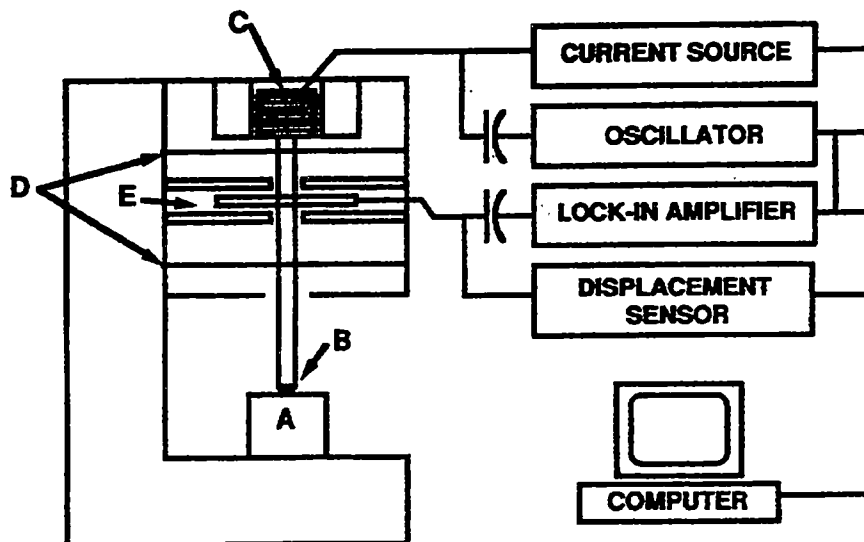


Figure 3. 2 A schematic diagram of the experimental apparatus used to perform the indentation experiments: (A) sample; (B) indenter; (C) load application coil; (D) indentation column guide springs; (E) capacitive displacement sensor[46].

Table 3. 1 Indentation Test Segments Used.

No	Type	Description
1	Approach	Find surface
2	Load	Load at 50 $\mu\text{N}/\text{sec}$ of load rate up to 1000 $\mu\text{N}$ toward 50 nm of contact depth
3	Hold	Hold the load for 10 seconds
4	Unload	Unload the applied load down to 90% at load rate
5	Load	Load at 200 $\mu\text{N}/\text{sec}$ of load rate up to 4000 $\mu\text{N}$ toward 100 nm of contact depth
6	Hold	Hold the load for 10 seconds
7	Unload	Unload the applied load down to 90% at load rate
8	Load	Load at 800 $\mu\text{N}/\text{sec}$ of load rate up to 16000 $\mu\text{N}$ toward 200 nm of contact depth
9	Hold	Hold the load for 10 seconds
10	Unload	Unload the applied load down to 90% at load rate
11	Hold	Hold segment designed to log 100 data points at two-second intervals
12	Unload	Unload completely at load rate

## CHAPTER 4

### RESULTS AND DISCUSSION

#### 4. 1 X-ray Diffraction of Titanium Nitride and Silicon Nitride Films

Titanium nitride films, for X-ray diffraction were deposited by PLD using a laser energy density of  $2.86 \text{ J/cm}^2$  at a repetition rate of 30 Hz for 1 hour. The X-ray diffraction pattern of titanium nitride target with  $2\theta$  in the range from  $30$  to  $70$  is shown in Figure 4. 1. (a). Figure 4. 2. (b) shows the diffraction pattern of the TiN film under the same condition as that used for the target. The three peaks located at  $2\theta$  values of  $36.57^\circ$ ,  $42.41^\circ$  and  $61.71^\circ$  were in identical positions for both film and target. They correspond to the (111), (200), and (220) of the face-centered structure for TiN. The measured lattice parameter was  $0.426 \text{ nm}$  and the JCPDS card indicates a  $0.424 \text{ nm}$  lattice parameter for the TiN. The lattice parameter is a good indicator of the stoichiometric composition of TiN. Intensity and width of each peak for titanium nitride film were smaller and wider than those of the target. The reason is that the grain size of the film was much smaller than that in the target as shown by TEM. The Scherrer Formula

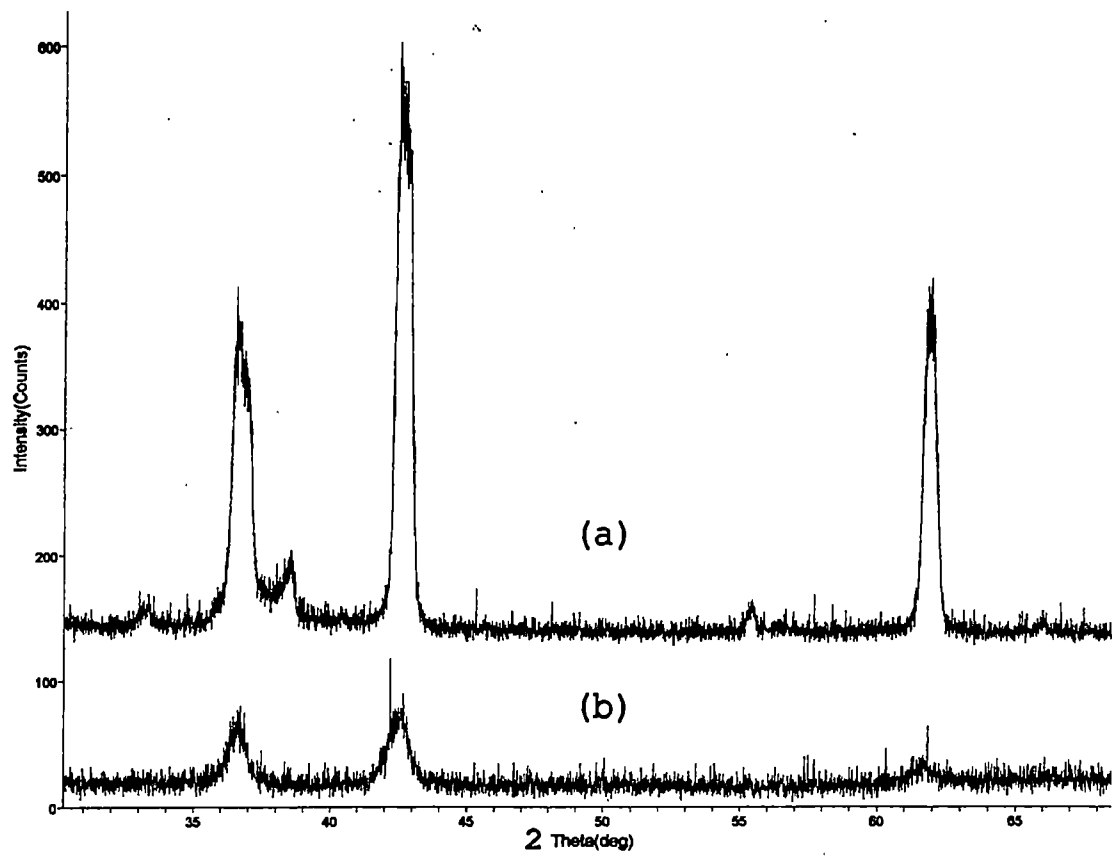


Figure 4. 1 XRD of a TiN target(a) and a TiN film(b) deposited at  $E_d = 2.86 \text{ J/cm}^2$ .

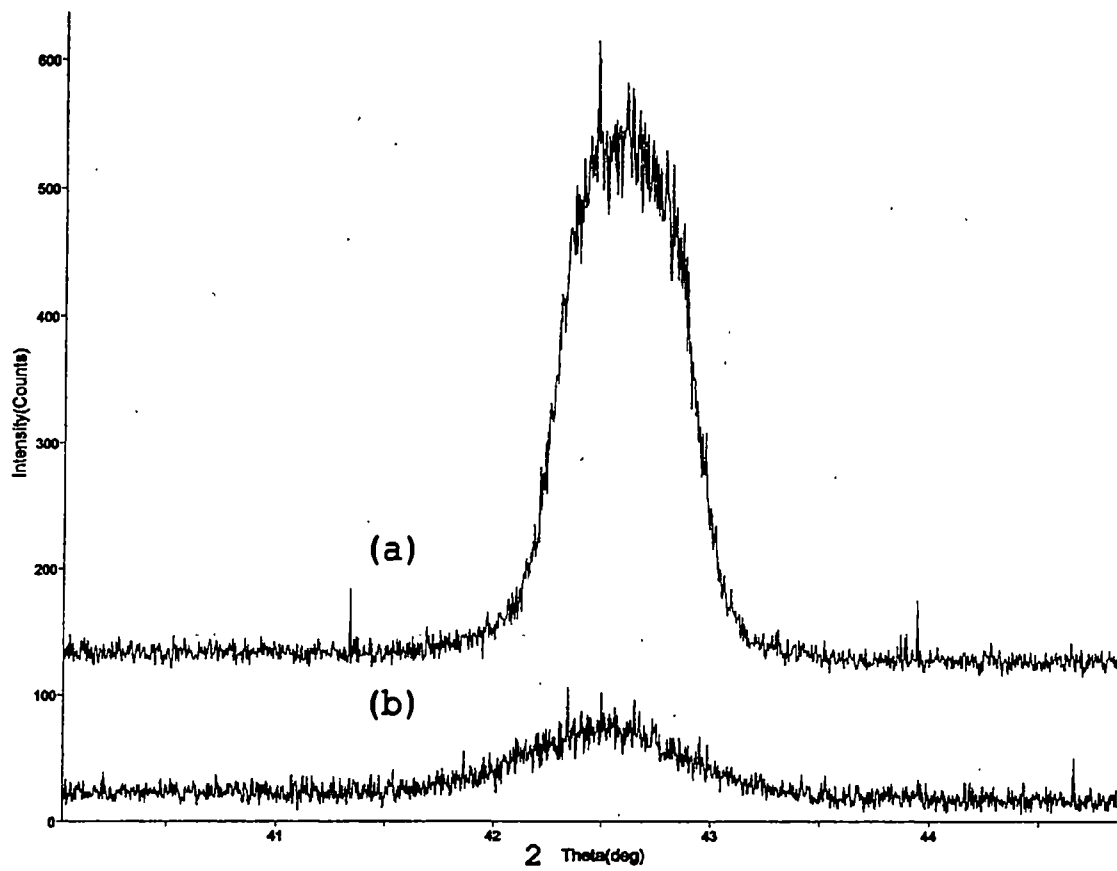


Figure 4. 2 XRD for (200) plane of a TiN target(a) and a TiN film(b) deposited at  $E_d = 2.86 \text{ J/cm}^2$ .

together FWHM of (200) reflection was used to estimated the grain size, that was 15.5 nm (Figure 4. 2. (b)). Silicon nitride films for X-ray diffraction were deposited by PLD using a laser energy density of 3 J/cm<sup>2</sup> for 20 minutes at a repetition rate of 20 Hz. Figure 4. 3. (a) and (b) show the X-ray diffraction patterns of silicon nitride target and film in the 2 $\theta$  range from 10° to 60°. The diffraction pattern indicates that the silicon nitride target has an  $\alpha$ -Si<sub>3</sub>N<sub>4</sub> structure (JCPDS # 40-1129). On the other hand, the silicon nitride film had a randomly oriented amorphous structure as shown in Figure 4. 3 (b).

#### **4. 2 Transmission Electron Microscopy**

Selected area diffractions (SAD) of 40 nm - thick titanium nitride and 40 nm - thick silicon nitride films are shown in Figure 4. 4 (a) and (b). Several clear ring patterns representing each crystalline family of planes indicated that titanium film deposited with 2.5 J/cm<sup>2</sup> in vacuum(P= 2\*10<sup>-7</sup> torr) at room temperature had a randomly oriented polycrystalline structure. This result agreed with the result of X-ray diffraction study. After calibration of the camera length, lattice parameter of crystal in the film was 0.426 nm that was close to that of bulk TiN(0.424

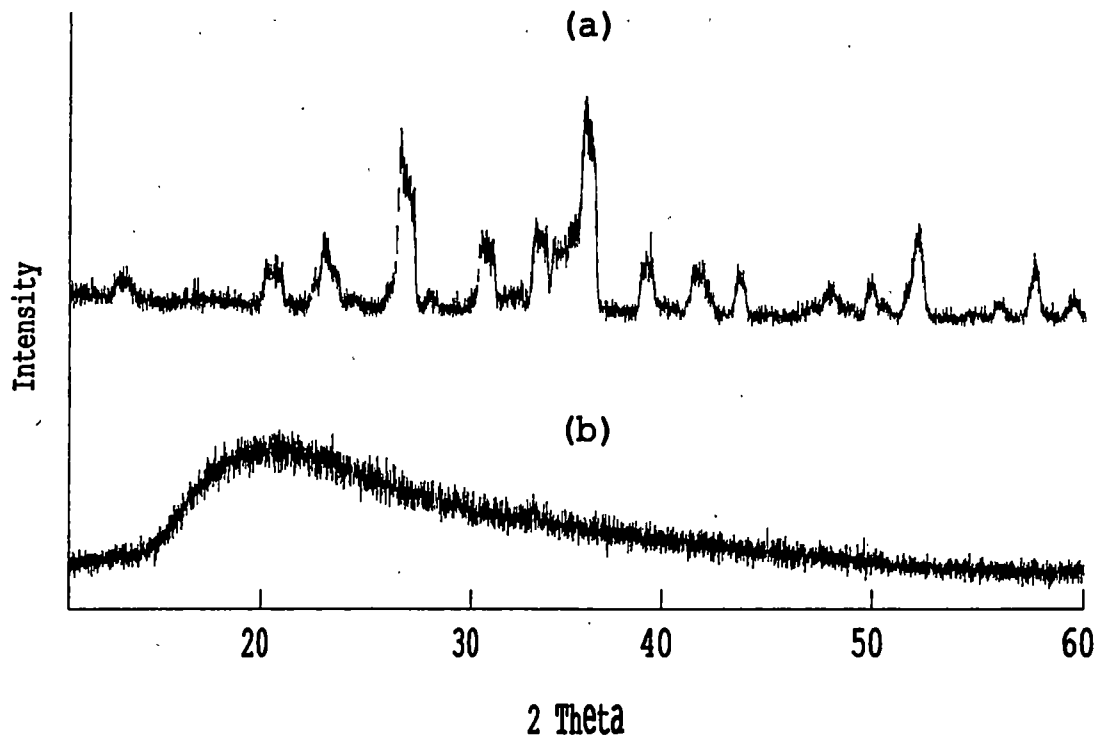
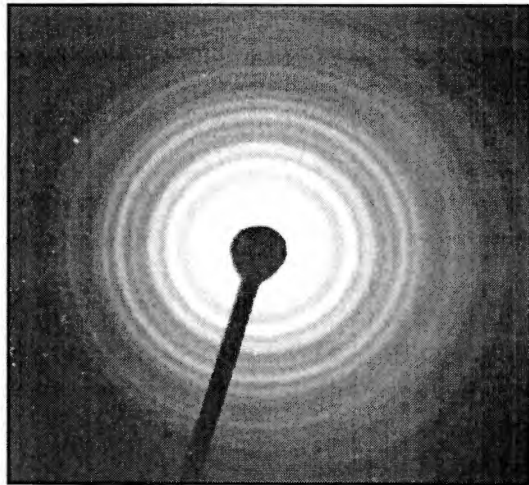


Figure 4. 3 XRD of a  $\text{Si}_3\text{N}_4$  target(a) and a  $\text{Si}_3\text{N}_4$  film(b) deposited at  $E_d = 3 \text{ J/cm}^2$ .



nm in JCPDS #38-1420). SAD of silicon nitride film deposited under the same condition as TiN film shows diffused ring pattern, which indicated this film had an amorphous structure, again in agreement with X-ray measurements.

The bright field image and EDS spectra of TiN film are shown in Figure 4. 5 (a) and (b). TiN/Si<sub>3</sub>N<sub>4</sub>(10 nm/40 nm) and TiN/Si<sub>3</sub>N<sub>4</sub>(20 nm/40 nm) composite films were also analyzed by TEM (Figure 4. 6 and 7). These films consist of randomly distributed nano-crystals of TiN. The amorphous silicon nitride film is not visible in these micrographs due to the lack of contrast. From these bright images, the grain size of each film was roughly determined as; 10 nm for TiN film (40 nm), 5 nm for TiN/Si<sub>3</sub>N<sub>4</sub> (10 nm/40 nm) film, and 7 nm for TiN/Si<sub>3</sub>N<sub>4</sub> (20 nm/40 nm) film. The grain size increased with the thickness of TiN film deposited.

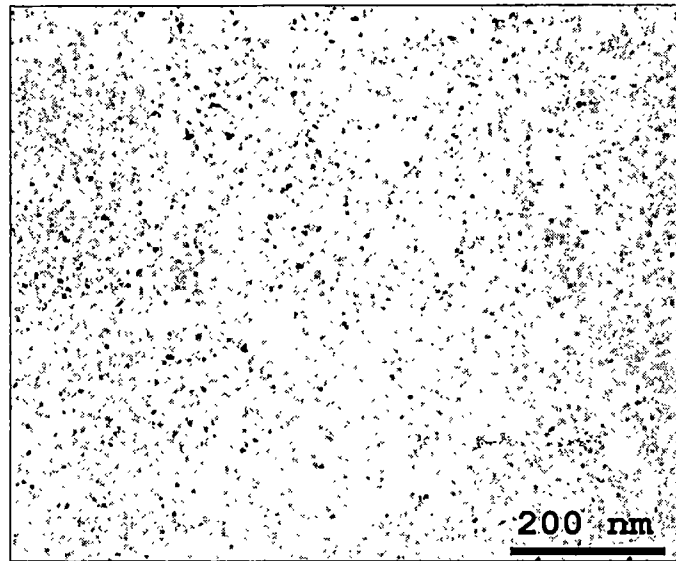


(a)

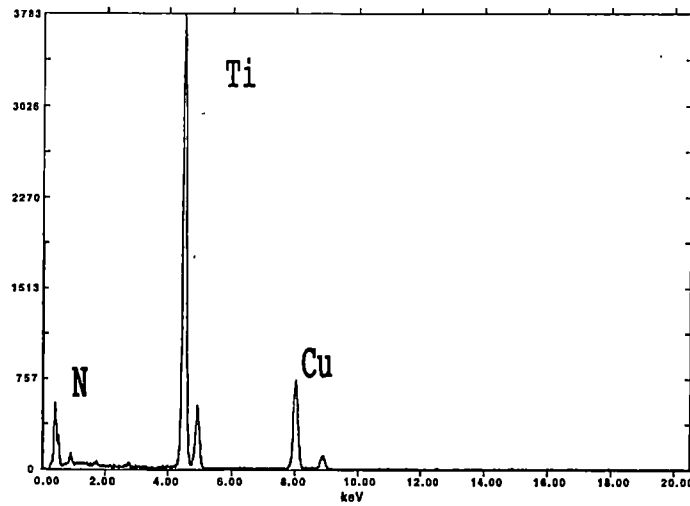


(b)

Figure 4. 4 SAD of a TiN film (a) and a Si<sub>3</sub>N<sub>4</sub> film (b) deposited at  $E_d = 2.5 \text{ J/cm}^2$ .

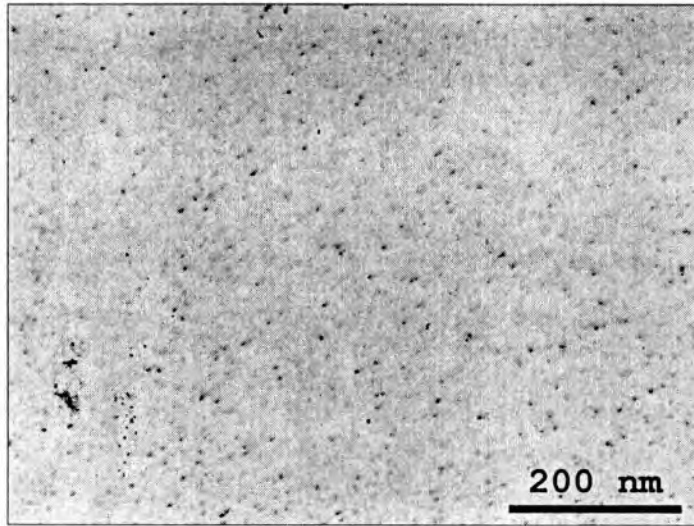


(a)

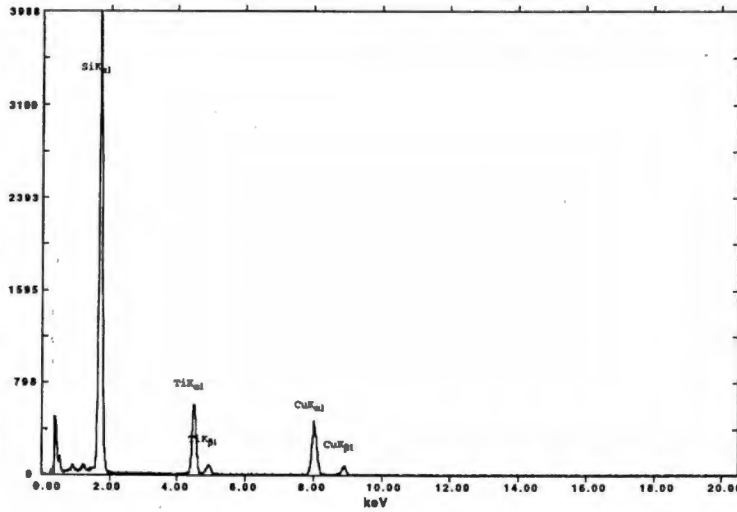


(b)

Figure 4.5 Bright field image (a) and EDS (b) of a TiN film (40 nm) deposited at  $E_d = 2.5 \text{ J/cm}^2$ .

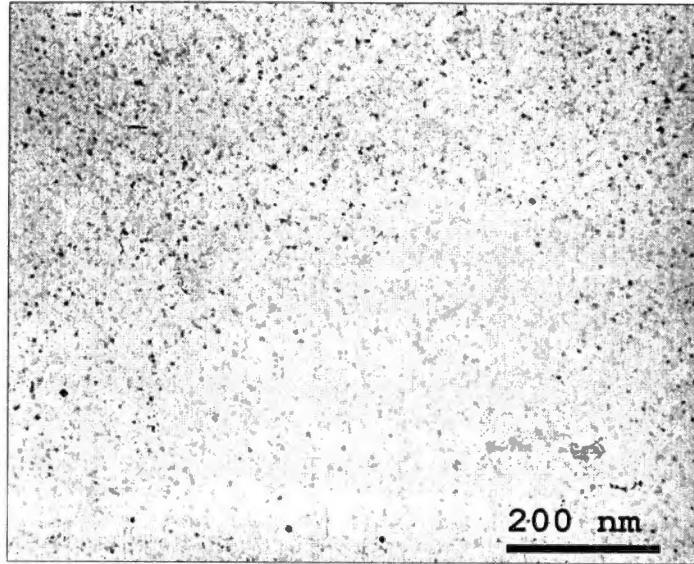


(a)

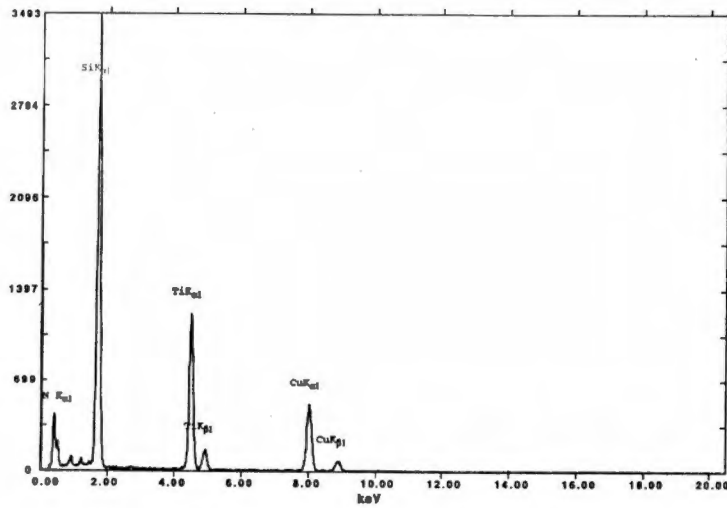


(b)

Figure 4.6 Bright field image (a) and EDS (b) of a  $\text{Si}_3\text{N}_4$  (40 nm) + TiN (10 nm) multilayer film deposited at  $E_d = 2.5 \text{ J/cm}^2$ .



(a)



(b)

Figure 4. 7 Bright field image (a) and EDS (b) of a  $\text{Si}_3\text{N}_4$  (40 nm) + TiN (20 nm) multilayer film deposited at  $E_d = 2.5 \text{ J/cm}^2$ .

#### 4. 3 Particulates of Silicon Nitride Film

Particulates with a size distribution were found in all films deposited by PLD. The particulate density was higher in  $\text{Si}_3\text{N}_4$  than in TiN films. It is important to find an appropriate deposition condition in order to avoid the deposition of particulates. Probably during PLD it is impossible to get rid of particulates completely[21]. Silicon nitride films were deposited at various conditions in order to determine the effect of laser energy density, distance between target and substrate, and repetition rate on the production of particulates.

SEM micrographs of silicon nitride films deposited with  $E_d = 1.8 \text{ J/cm}^2$ ,  $2.5 \text{ J/cm}^2$ , and  $3.15 \text{ J/cm}^2$  in vacuum ( $P=1.6 \sim 2.0 \times 10^{-7}$  torr) are shown in Figure 4. 8, 9, and 10. In these experiments the distance between target and substrate was maintained constant at about 4 cm. There were no significant differences in the density and size of particulates on the silicon nitride films deposited with  $E_d = 1.8 \text{ J/cm}^2$  and  $2.5 \text{ J/cm}^2$ . A few large particulates in the range of  $4 \sim 5 \mu\text{m}$  were observed in both films. However, the film deposited with  $E_d = 3.15 \text{ J/cm}^2$  had higher density of particulates than those on films deposited with  $E_d = 1.8 \text{ J/cm}^2$  or  $2.5 \text{ J/cm}^2$ . Also this film had much larger

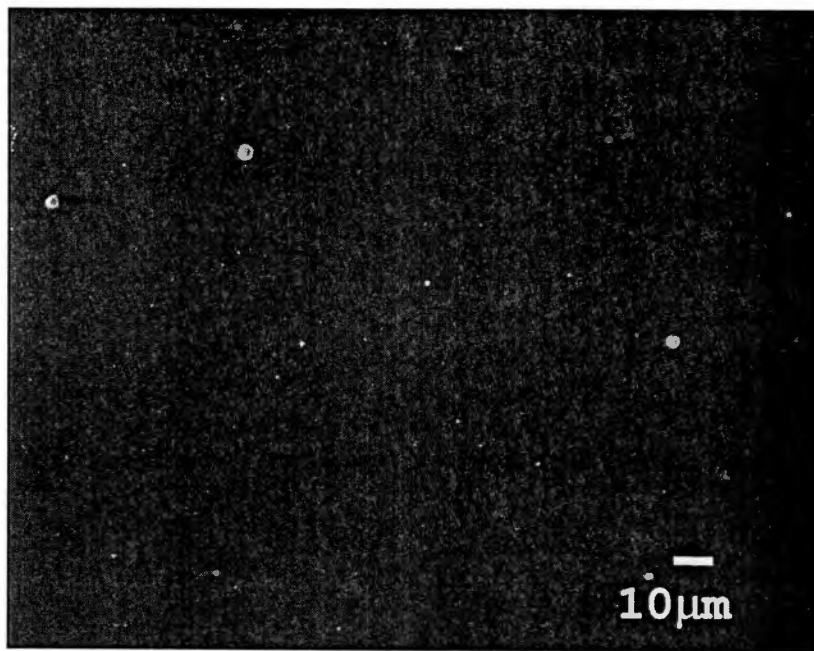


Figure 4. 8 SEM micrograph of a silicon nitride film deposited for 5000 pulses at  $E_d = 1.8 \text{ J/cm}^2$ . The repetition rate was 10 Hz and the target-substrate distance was 4 cm.

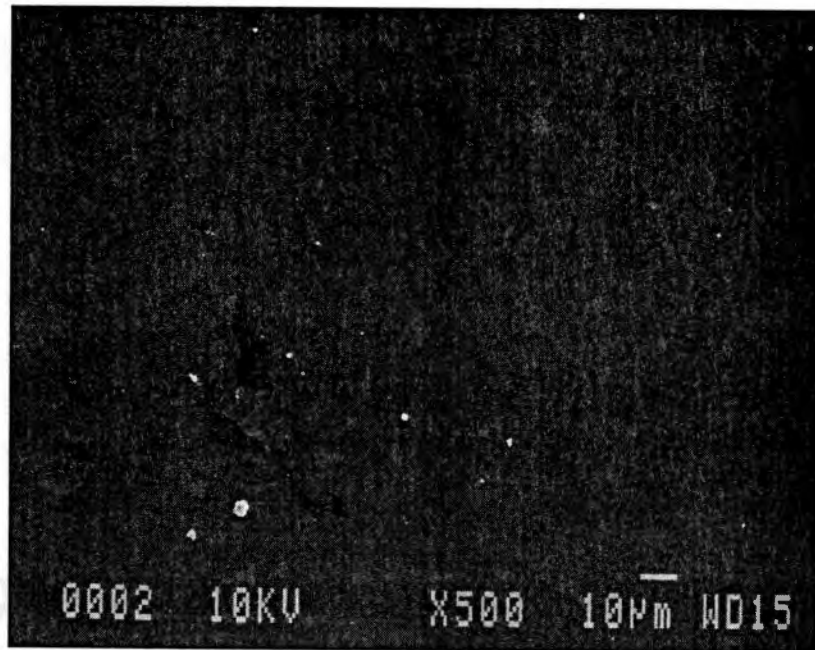


Figure 4. 9 SEM micrograph of a silicon nitride film deposited for 5000 pulses at  $E_d = 2.5 \text{ J/cm}^2$ . The repetition rate was 10 Hz and the target-substrate distance was 4 cm.



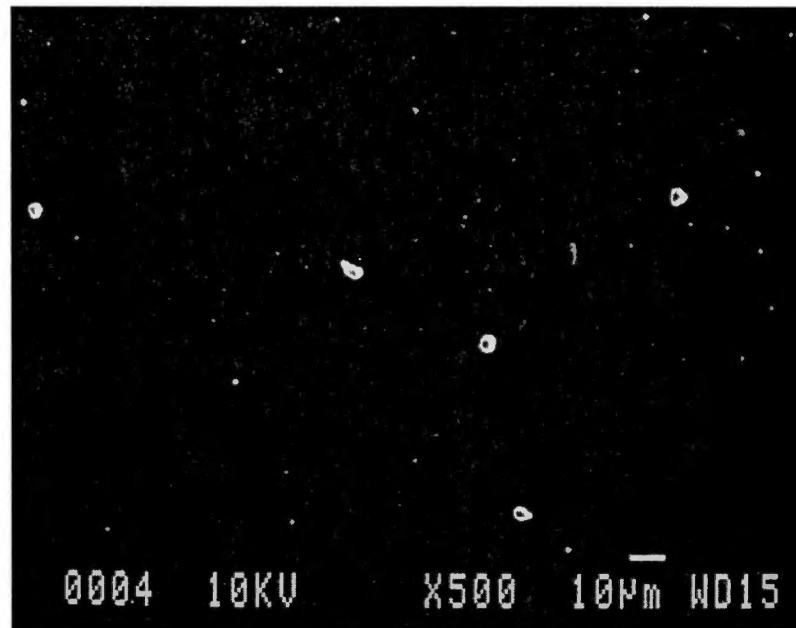


Figure 4. 10 SEM micrograph of a silicon nitride film deposited for 5000 pulses at  $E_d = 3.15 \text{ J/cm}^2$ . The repetition rate was 10 Hz and the target-substrate distance was 4 cm.

particulates ranging from 7 to 9  $\mu\text{m}$ .  $E_d = 1.8 \text{ J/cm}^2$ ,  $2.5 \text{ J/cm}^2$ , and  $3.15 \text{ J/cm}^2$  were above threshold energy density for formation of particulate. As the laser fluence increases the density and size of the particulates tend to a saturation value. The increase in particulate size and density with increasing laser fluence observed in silicon nitride agrees well with the result of YBCO film produced by XeCl laser[22]. Higher fluence promotes higher etching rates and more craters. The fracture of the crater edges promotes the formation of large and irregular-shaped particulates.

Two more silicon nitride films were deposited with the same energy density and distance from target to substrate ( $E_d = 2.5 \text{ J/cm}^2$ ,  $d = \sim 4 \text{ cm}$ ) but at repetition rate of 20 Hz in one film and 30 Hz in the other. The film deposited at 10 Hz had less particulates than those deposited at 20 Hz or 30 Hz of repetition rate. The particulates density for both films deposited at 20 Hz and 30 Hz was almost the same. However, there was difference in particulate size, the film deposited at 20 Hz had slightly larger particulates than the film deposited at 30 Hz.

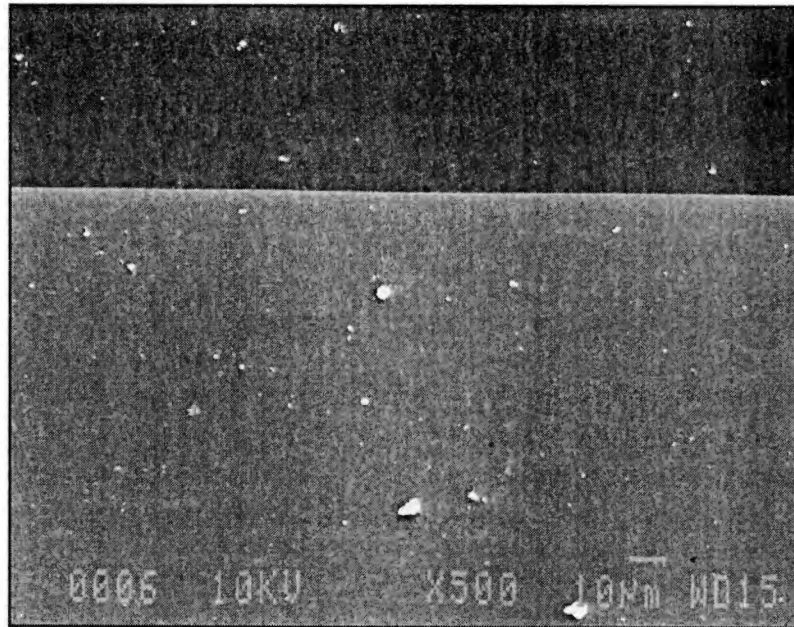


Figure 4. 11 SEM micrograph of a silicon nitride film deposited for 5000 pulses at  $E_d = 2.5 \text{ J/cm}^2$ . The repetition rate was 20 Hz and the target-substrate distance was 4 cm.

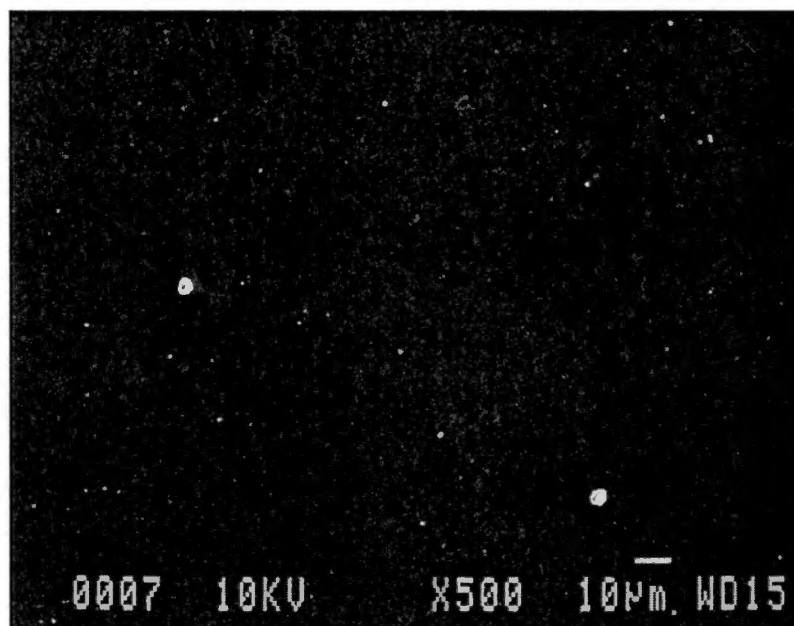
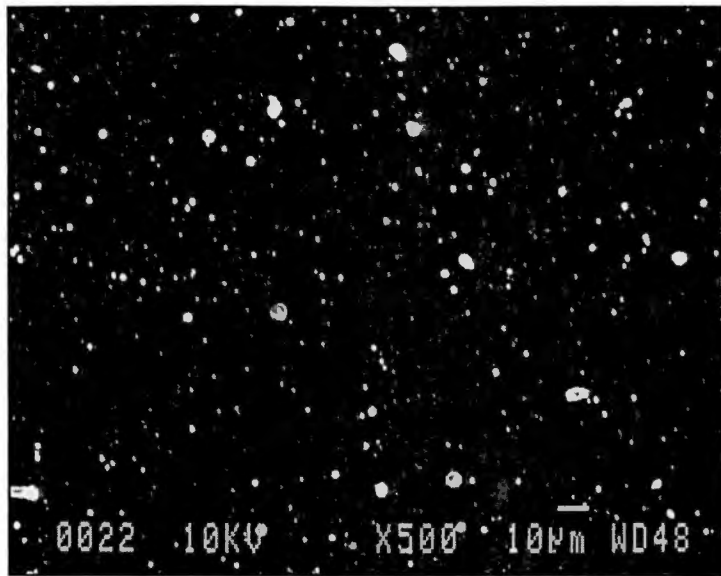


Figure 4. 12 SEM micrograph of a silicon nitride film deposited for 5000 pulses at  $E_d = 2.5 \text{ J/cm}^2$ . The repetition rate was 30 Hz and the target-substrate was 4 cm.

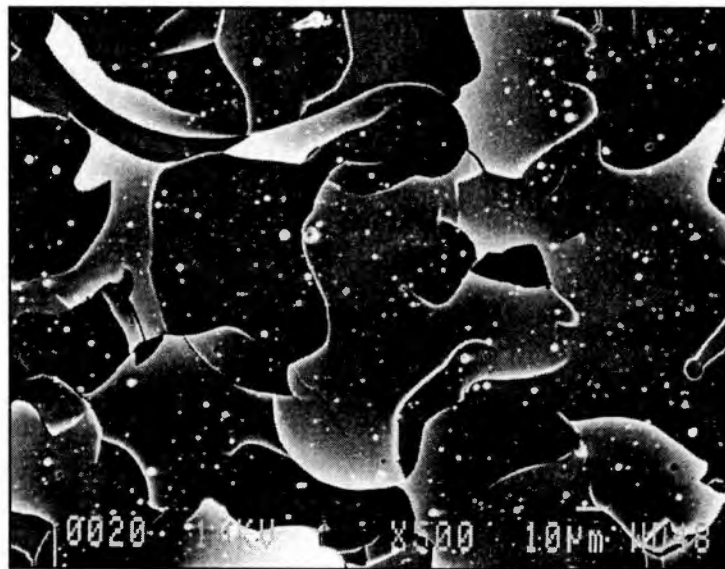
Films were deposited with the same energy density ( $E_d = 2.5 \text{ J/cm}^2$ ) and repetition rate (10 Hz) but varying the distance between target and substrate. The film deposited with  $d = 2 \text{ cm}$  had the highest density of particulates as shown in (Figure 4. 13. (a)). This film has partially broken areas on which many particulates can be observed (Figure 4. 13 (b)). Residual stress generated is probably responsible for the film fracture. The density of particulates decreased with increase in distance.

It should be noticed that the film with  $d = 5 \text{ cm}$  had a larger number of large particulates ranging of  $5 \sim 8 \mu\text{m}$  than those in the film deposited with  $d = 6 \text{ cm}$ . The film with  $d = 5 \text{ cm}$  was deposited with a target that was used for many experiments. The shape of particulates on this film is not spherical but very irregular; large and irregular shape of the particulates seemed to be caused by solid ejecta[21] from the groove on the target resulting from the continuous use of the laser.

The deposition rate of silicon nitride films as a function of the distance between target and substrate is shown in Figure 4. 16. These films were deposited with  $E_d = 2.5 \text{ J/cm}^2$  at a repetition rate of 10 Hz in vacuum. The deposition rate increased with decreasing in distance



(a)



(b)

Figure 4. 13 SEM micrograph of a silicon nitride film deposited for 5000 pulses at  $E_d = 2.5 \text{ J/cm}^2$ . The repetition rate was 10 Hz and the target-substrate distance was 2 cm.

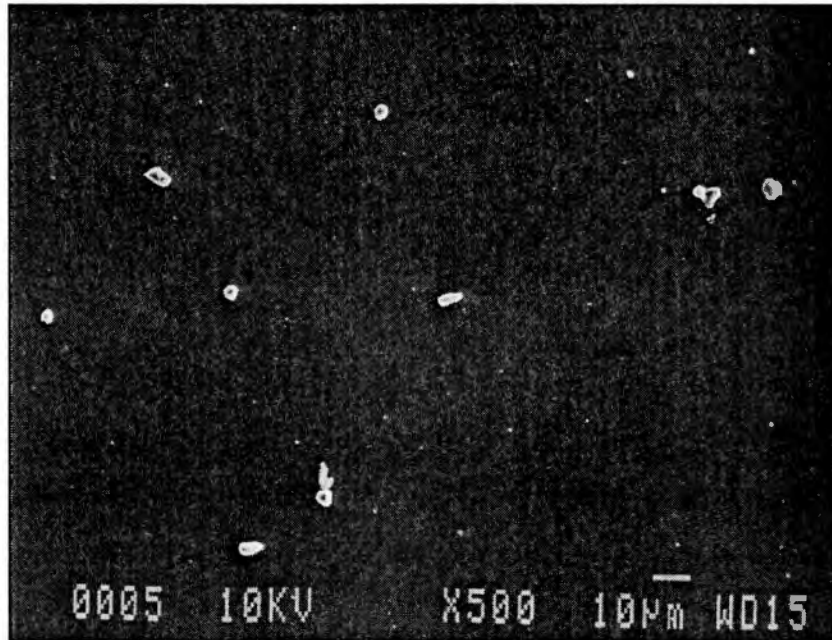


Figure 4. 14 SEM micrograph of a silicon nitride film deposited for 5000 pulses at  $E_d = 2.5 \text{ J/cm}^2$ . The repetition rate was 10 Hz and the target-substrate distance was 5 cm.

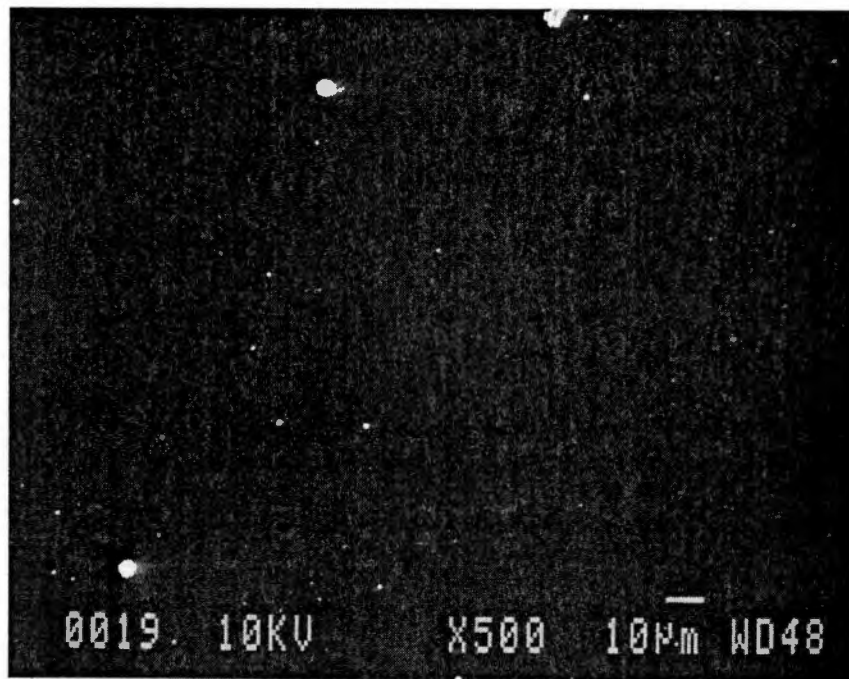


Figure 4. 15 SEM micrograph of a silicon nitride film deposited for 5000 pulses at  $E_d = 2.5 \text{ J/cm}^2$ . The repetition rate was 10 Hz and the target-substrate distance was 6 cm.



between target and substrate. The deposition rate at 2 cm was 1.28 Angstrom/pulse that was sixteen times larger than that at 6 cm.

The deposition rates of films with  $E_d = 1.8, 2.5,$  and  $3.15 \text{ J/cm}^2$  at the same distance of 4 cm and repetition rate of 10 Hz were 0.02 nm/pulse, 0.022 nm/pulse, and 0.026 nm/pulse, respectively. The deposition rates of films with  $E_d = 2.5$  at repetition rate of 20 Hz and 30 Hz were 0.28 Angstrom/pulse and 0.24 Angstrom/pulse, respectively. This decrease of deposition rate from 20 to 30 Hz is thought that the plasma generated by the continuous pulse (30 pulses/second) remains shielding the target from the following pulse. The plasma shielding has been known as one of the mechanisms that reduce the ablation rate[49].

### Deposition Rate vs. Distance for Si<sub>3</sub>N<sub>4</sub> Film

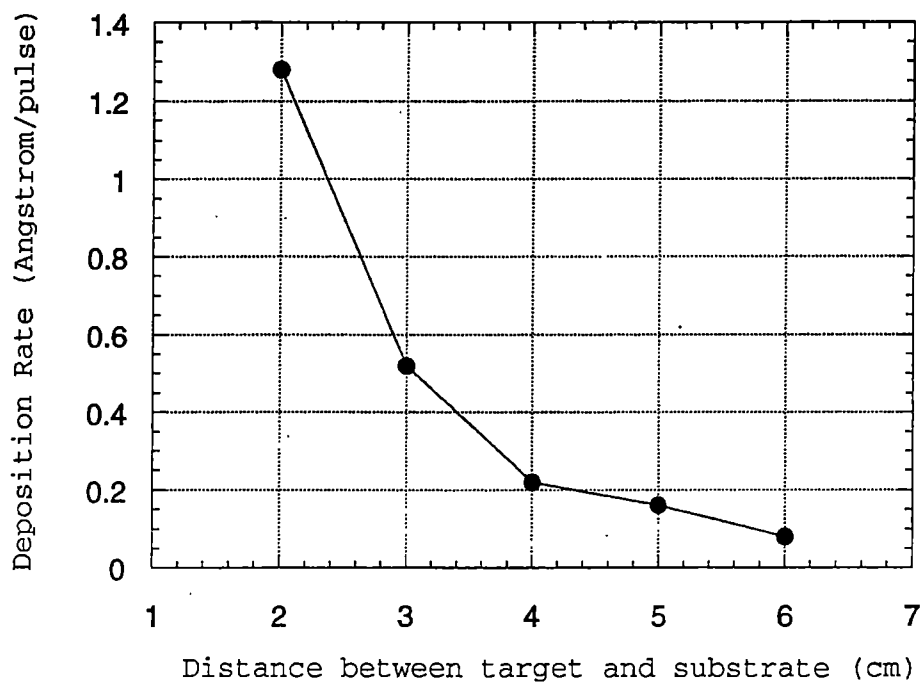


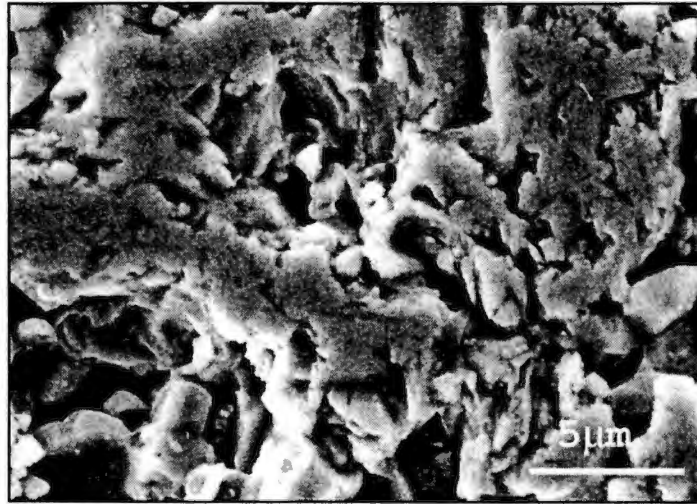
Figure 4. 16 Deposition rate as a function of the target-substrate distance for 5000 pulses at  $E_d = 2.5 \text{ J/cm}^2$ . The repetition rate was 10 Hz.

#### 4. 4 Effect of Laser Ablation on Targets

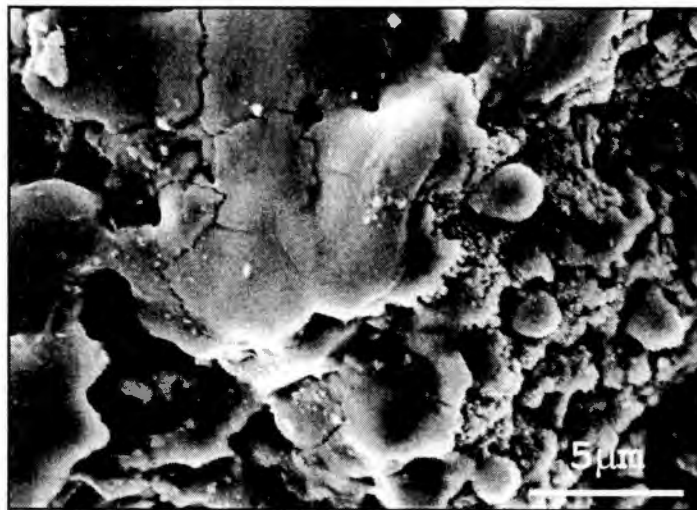
The laser beam impinging on the targets changes both morphology and chemical composition of titanium and silicon nitrides. Changes in deposition rate with use prompt us to closely examine the targets.

Figure 4. 17 shows the SEM morphology of titanium nitride target polished(a) and ablated(b) for 25,000 pulses with  $E_d = 2.5 \text{ J/cm}^2$  at 20 Hz. As shown by SEM, the ablated titanium nitride target was covered by molten regions on the surface. There were also present microcracks probably due to the high cooling rate. A few particulates ranging of 100 ~ 300 nm were observed on the target. These particulates seem to be re-deposited titanium nitride from the substrate. As the irradiation proceeds, the color of the irradiated area changed from gold to white. It seems that this color change is due to the formation of nonstoichiometric titanium oxy-nitride species resulting from the reaction between titanium nitride and residual oxygen in the chamber[50, 51]. However the composition of the TiN film is very close to stoichiometry as indicated by XRD.

Cones developed on  $\text{Si}_3\text{N}_4$  target after irradiation with  $E_d = 2.5 \text{ J/cm}^2$  after 25000 shots of pulse (Figure 4. 18).



(a)



(b)

Figure 4. 17 SEM morphology of the titanium nitride target polished(a) and ablated(b) for 25,000 pulses at  $E_d = 2.5$  J/cm<sup>2</sup>.

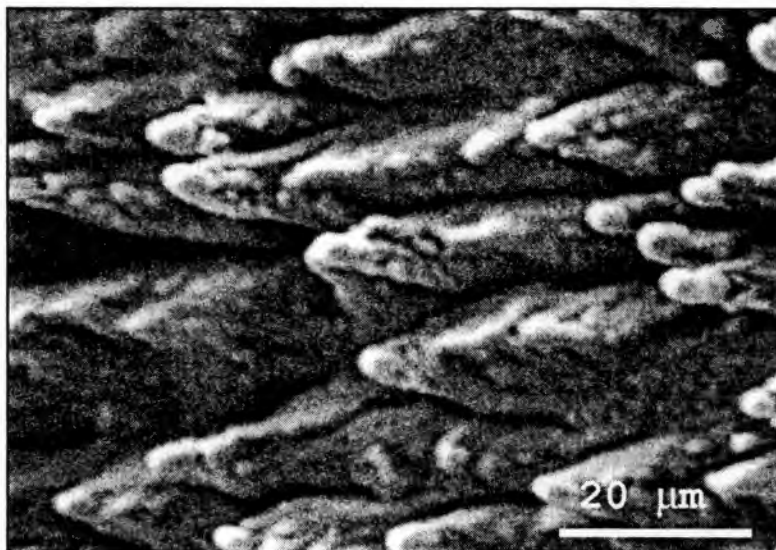


Figure 4. 18 SEM morphology of the silicon nitride target after being ablated for 25,000 pulses at  $E_d = 2.5 \text{ J/cm}^2$ .

The length and diameter of a cone were  $6 \sim 10 \mu\text{m}$  and  $3 \sim 4 \mu\text{m}$ , respectively. The cones were aligned along the direction of incident laser beam ( $\sim 45^\circ$ ). As shown in Figure 4. 19, a few cones were higher than base  $\text{Si}_3\text{N}_4$  target surface. It seems that some materials were re-deposited after decomposition of the target.

Miyamoto and Maruo[52] reported that surface with cones was observed in excimer laser processing of  $\text{Si}_3\text{N}_4$ . They proposed that small fragments of Si from the decomposition of  $\text{Si}_3\text{N}_4$  are re-deposited on the target. Since the reflectivity of Si at 248 nm is much larger than that of  $\text{Si}_3\text{N}_4$ , only  $\text{Si}_3\text{N}_4$  surface without Si fragments reach the threshold for ablation of decomposition. Once removal of  $\text{Si}_3\text{N}_4$  begins, tilted faces produce cones. At larger than  $5 \text{ J/cm}^2$ , even the area covered with Si fragments reach the ablation threshold leading to smooth surface.

XPS scans for polished(a) and ablated(b)  $\text{Si}_3\text{N}_4$  target with  $E_d = 2.5 \text{ J/cm}^2$  for 25000 pulses are shown in Figure 4. 20. The higher Cls peak in polished target(a) was thought due to the contamination by ethanol and acetone during the cleaning of the target. The relative content of nitrogen and silicon were determined from the intensity ratio of each core level; Si 2p3 for silicon and N 1s for nitrogen.

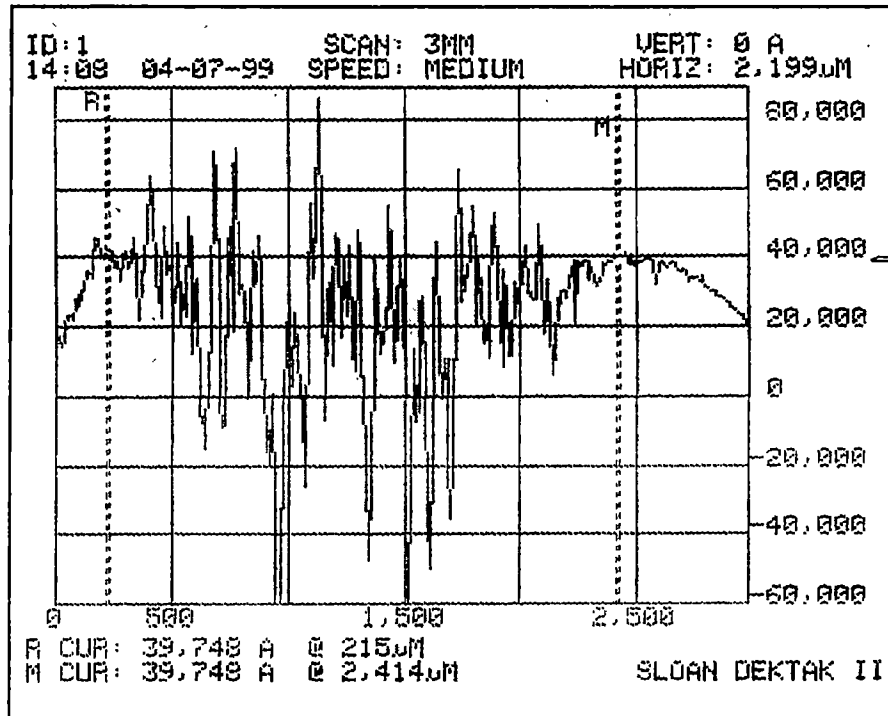


Figure 4. 19 A Dektak II profilometer of the silicon nitride target being ablated for 25000 pulses at  $E_d = 2.5$  J/cm<sup>2</sup>. The vertical scale is in micrometer and the horizontal scale is Angstrom.

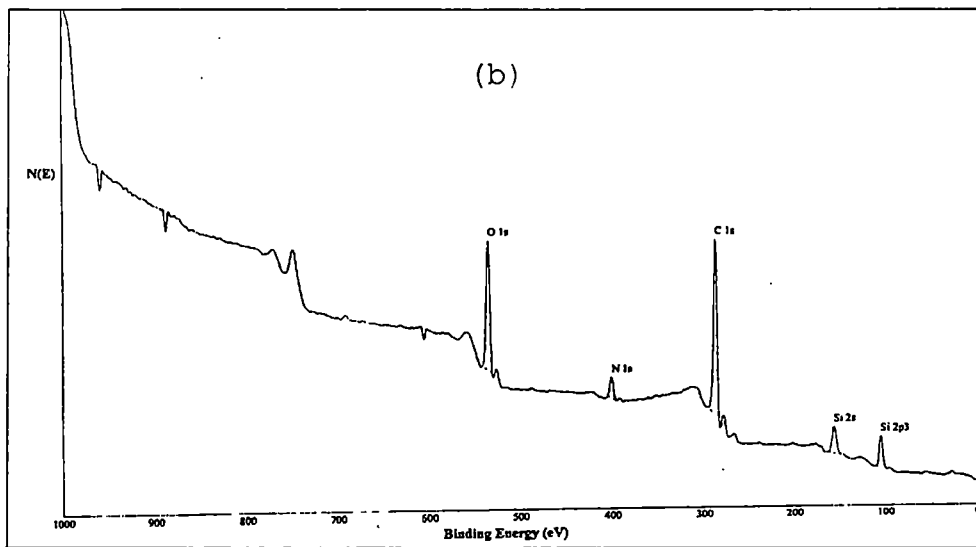
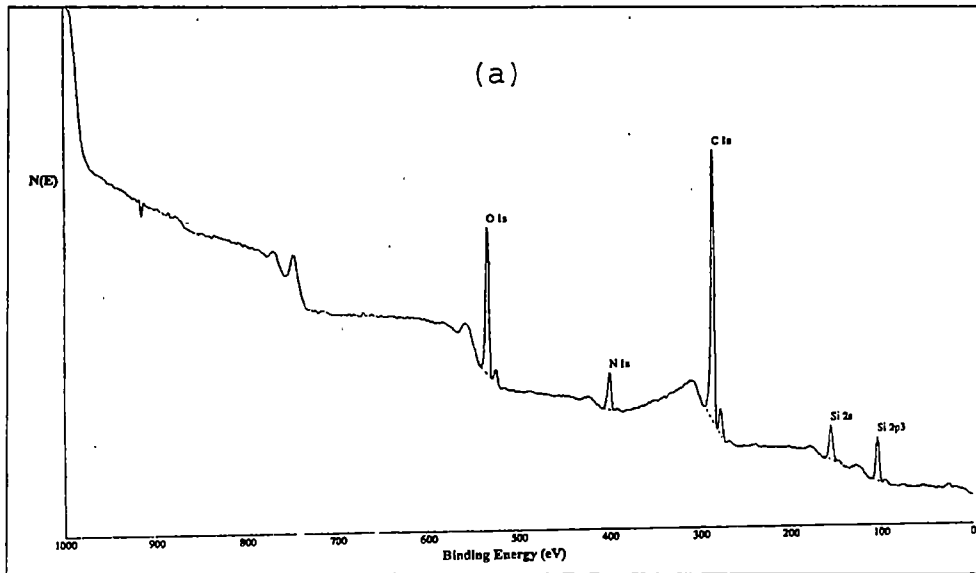


Figure 4. 20 XPS survey spectrum of the polished silicon nitride target(a) and the ablated silicon nitride target(b) for 25,000 pulses at  $E_d = 2.5 \text{ J/ cm}^2$ .



The binding energy of Si 2p3 for polished target was 102.2 eV, which is close to the values[53,54] reported for Si in a Si<sub>3</sub>N<sub>4</sub> environment whereas that for ablated target was 100.7 eV close to that of silicon in a silicon environment. The content of nitrogen for ablated target was 25% smaller than that for polished target. The cones produced by ablation of laser with 2.5 J/cm<sup>2</sup> had less nitrogen than did original silicon nitride target without laser-treatment.

#### 4. 5 Hardness and Elastic Modulus of Titanium Nitride Film and Silicon Nitride Film

The hardness and elastic modulus of titanium nitride film, silicon nitride film, and multi-layered film were measured using a Nanoindenter ® II which is able to measure the indentation load and depth during the indentation.

The films for indentation were deposited at  $E_d = 2.5$  J/cm<sup>2</sup> at 20 Hz and a target-substrate distance of 4 cm. The deposition process was performed at room temperature in vacuum ( $1 \sim 2 * 10^{-7}$  torr) and at 500 °C in nitrogen atmosphere ( $1 \sim 2 * 10^{-3}$  torr). The total thickness of each film was about 500 nm. Four specimens in both conditions were prepared as follows: TiN film (500 nm), Si<sub>3</sub>N<sub>4</sub> film (500 nm), Multi-layered film (layers consisting of TiN 10 nm + Si<sub>3</sub>N<sub>4</sub> 3 nm), Multi-layered film (layers consisting of TiN 10 nm + Si<sub>3</sub>N<sub>4</sub> 1 nm). The hardness and elastic modulus at a contact depth of 30 nm were regarded as representative of the film.

The hardness as a function of contact depth for samples deposited at room temperature in vacuum is shown in Figure 4. 21. Titanium nitride film had the highest hardness among samples followed by a multi-layered film

## Hardness vs. Contact Depth

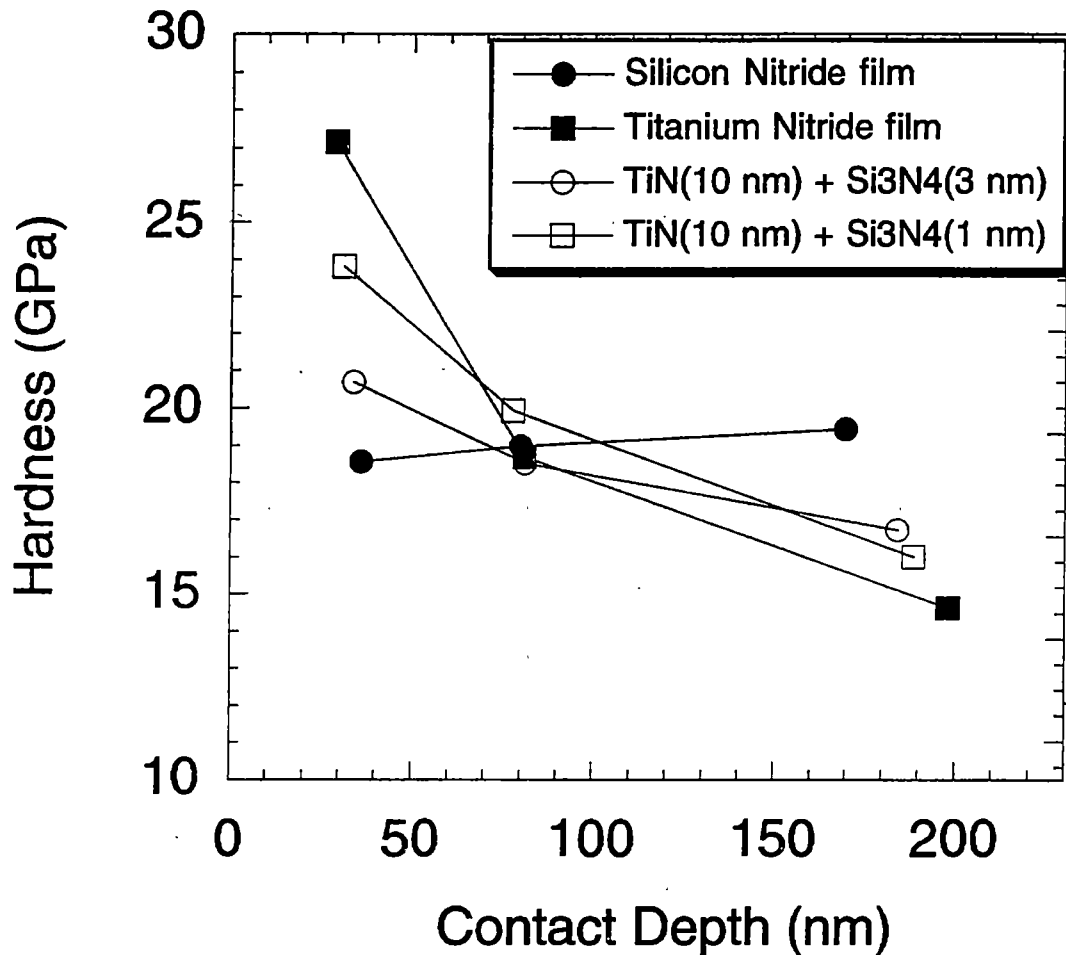


Figure 4. 21 Hardness as a function of contact depth for films deposited at  $E_d = 2.5 \text{ J/cm}^2$ . The repetition rate was 20 Hz and the target-substrate distance was 4 cm. The depositions were performed at room temperature in vacuum.

(TiN 10 nm + Si<sub>3</sub>N<sub>4</sub> 1 nm). The hardness of titanium nitride film was about  $26 \pm 4$  GPa. The hardness of silicon nitride film was  $19 \pm 0.9$  GPa. Both values of titanium nitride film and silicon nitride film were slightly higher than values of bulk materials reported in the literature; 2100 HV for TiN and 1720 HV for Si<sub>3</sub>N<sub>4</sub> [28]. The hardness of titanium nitride film was 10 GPa higher than microhardness of titanium nitride film deposited using XeCl excimer laser[11]. However, silicon nitride film had a lower hardness than that of silicon nitride film produced in nitrogen environment at 700 °C using KrF excimer laser[12]. The hardness of the multi-layered film (TiN 10 nm + Si<sub>3</sub>N<sub>4</sub> 1 nm)having more TiN, which had the highest hardness value, was close to the value of titanium nitride whereas that of the multi-layered film (TiN 10 nm + Si<sub>3</sub>N<sub>4</sub> 3 nm)having more silicon nitride was close to silicon nitride.

The elastic modulus of four samples as a function of the contact depth is plotted in Figure 4. 22. The Elastic modulus of the titanium nitride film was  $265 \pm 25$  GPa that is about half of that of bulk titanium nitride reported in the literature; 590 GPa[28]. The multi-layered film composed of layers of TiN 10 nm + Si<sub>3</sub>N<sub>4</sub> 1 nm had an elastic modulus of  $264 \pm 21$  GPa, almost the same as the elastic

## Elastic Modulus vs. Contact Depth

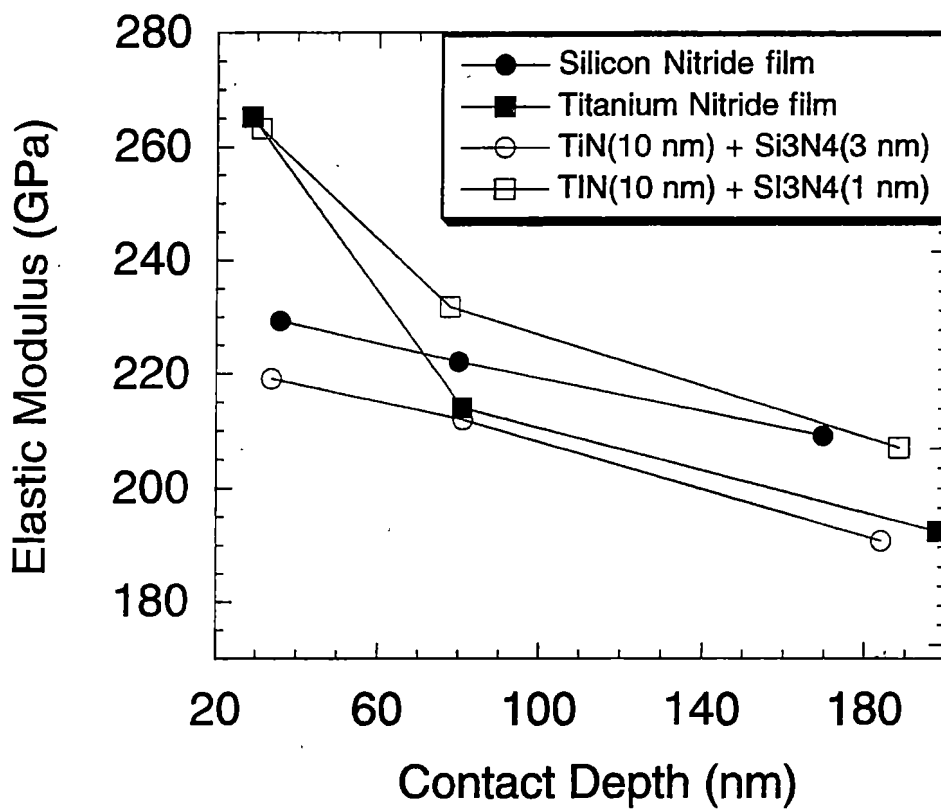


Figure 4. 22 Elastic modulus as a function of contact depth for films deposited at  $E_d = 2.5 \text{ J/cm}^2$ . The repetition rate was 20 Hz and the target-substrate distance was 4 cm. The depositions were performed at room temperature in vacuum.

modulus of the TiN film. The Elastic modulus of silicon nitride film was  $230 \pm 21$  GPa slightly higher than E of bulk silicon nitride reported in the literature; 210 GPa[28]. The Multi-layered film having layers of TiN 10 nm + Si<sub>3</sub>N<sub>4</sub> 3 nm had the lowest elastic modulus of the four films, a value close to that of the silicon nitride film.

The hardness as a function of contact depth for four samples deposited at 500 °C in nitrogen environment, silicon (100) wafer, and fused quartz is shown in Figure 4. 23. At variance with the titanium nitride film deposited at room temperature in vacuum, the hardness of titanium nitride film deposited at high temperature in  $10^{-3}$  torr of N<sub>2</sub> has the lowest hardness of the four specimens. This hardness is even lower than that reported in the literature for bulk TiN. The hardness of the TiN film deposited in this condition is ~ 10 GPa lower than that of titanium nitride film deposited at room temperature in vacuum. As shown previously, TiN film deposited at room temperature has a nano-crystalline structure. Since the larger grain size the lower hardness, the increase in particle size TiN film grown at 500 °C might be one of the reasons for lower hardness relative to titanium nitride film deposited at room temperature. XPS data for titanium nitride films

### Hardness vs. Contact Depth

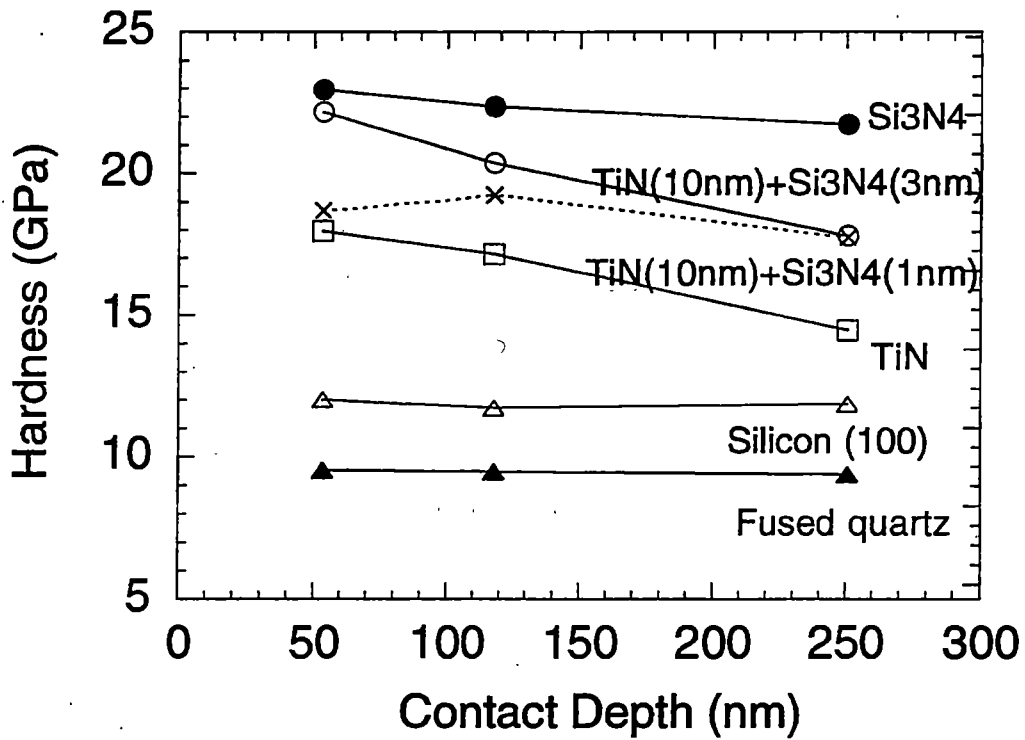


Figure 4. 23 Hardness as a function of contact depth for films deposited at  $E_d = 2.5 \text{ J/cm}^2$ . The repetition rate was 20 Hz and the target-substrate distance was 4 cm. The depositions were performed at 500 °C in nitrogen atmosphere ( $1 \sim 2 \times 10^{-3}$  torr).

generated in both conditions are shown in Figure 4. 24. (a) and (b). These data were compared with the standard TiN data that was TiN target with purity of 99.5 %. Both films had oxygen and carbon that might be resulted from oxidation and contamination as normally all films exposed to air have. After including in calculation the sensitivity factors for Ti  $2p_{3/2}$  and N 1s from a TiN standard, the relative ratio of  $[N]/[Ti]$  in the film was 0.724 for TiN grown at room temperature in vacuum and 0.370 for TiN grown at 500 °C in  $N_2$  atmosphere. The deposition of titanium nitride at 500 °C in nitrogen environment ( $10^{-3}$  torr) produced more nitrogen-deficient film that had a lower hardness. Thus, the concentration of nitrogen seemed have a main effect on the hardness of titanium nitride film. The hardness of silicon nitride film produced at 500 °C was  $23 \pm 0.8$  GPa, which is  $\sim 6$  GPa larger than that of titanium nitride deposited at the same condition and was higher than that of silicon nitride grown at room temperature. Unlike amorphous silicon nitride at room temperature, the silicon nitride film deposited at 500 °C has a crystalline structure. XRD of two silicon nitride films deposited at room temperature and 500 °C is shown in Figure 4. 25 (a) and



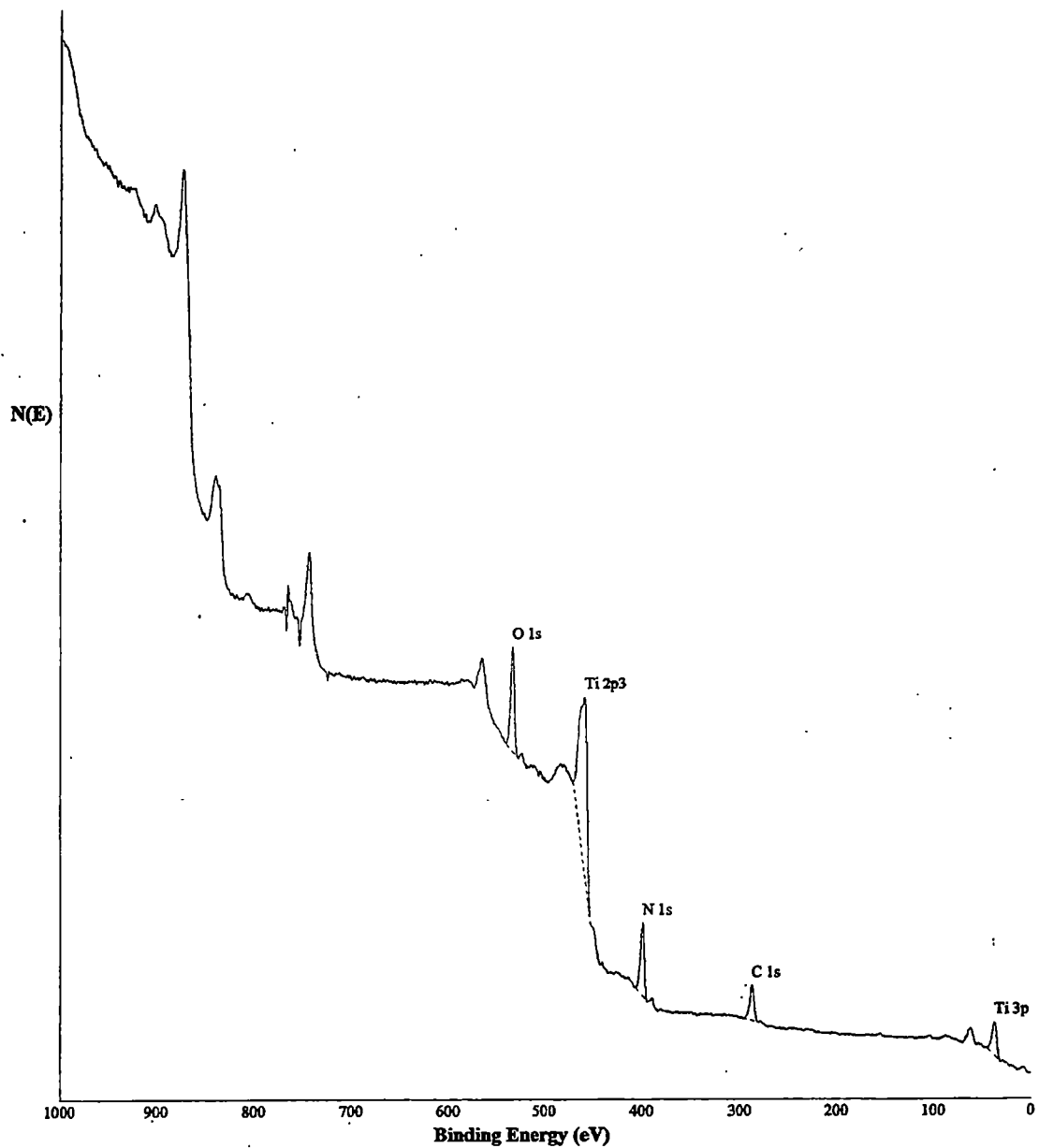


Figure 4. 24. (a) XPS survey spectrum of the titanium nitride film deposited with  $E_d = 2.5 \text{ J/cm}^2$  at room temperature in vacuum. The repetition rate was 20 Hz and the target- substrate distance was 4 cm.

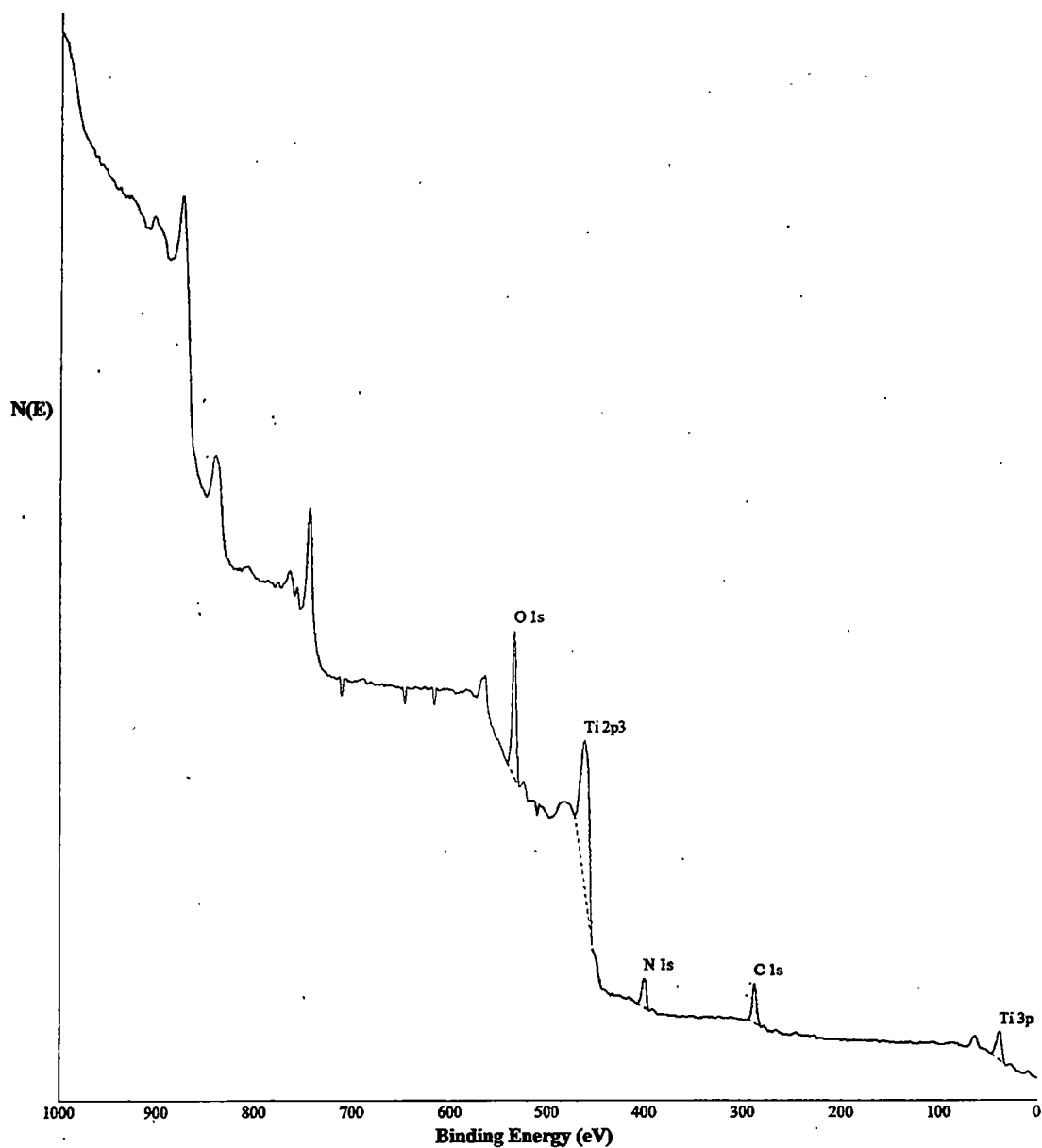


Figure 4. 24. (b) XPS survey spectrum of the titanium nitride film deposited with  $E_d = 2.5 \text{ J/cm}^2$  at  $500 \text{ }^\circ\text{C}$  in  $\text{N}_2$  ( $1 \sim 2 \times 10^{-3} \text{ torr}$ ). The repetition rate was 20 Hz and the target- substrate distance was 4 cm.

(b). Probably 500 °C was not high enough to crystallize silicon nitride completely. There were two distinct peaks in the  $2\theta$  range from 10° to 60°, but they were not sharp as shown in complete crystalline. Another possible reason for broadening of XRD peaks is the effect of very fine grain size. In fact the increase in hardness observed in film deposited at 500 °C may due to the formation of very small crystallites as detected by XRD. XPS data for silicon nitride films generated in both conditions are shown in Figure 4. 26. (a) and (b). These data were compared with the standard  $\text{Si}_3\text{N}_4$  data that was  $\text{Si}_3\text{N}_4$  target with purity of 99.9%. As mentioned in titanium nitride films, oxygen and carbon were detected in both silicon nitride films. After adopting the sensitivity factors for Si 2p and N 1s from the standard, the relative ratio of  $[\text{N}]/[\text{Si}]$  in the film was 1.16 for film grown at room temperature in vacuum, and 1.28 for film grown at 500 °C in a  $\text{N}_2$  atmosphere. The ratio of  $[\text{N}]$  to  $[\text{Si}]$  for silicon nitride produced at 500 °C in nitrogen atmosphere was close to 1.33 for the stoichiometric silicon nitride ( $\text{Si}_3\text{N}_4$ ). The deposition of silicon nitride at 500 °C in nitrogen environment ( $10^{-3}$  torr) generated film containing more nitrogen.

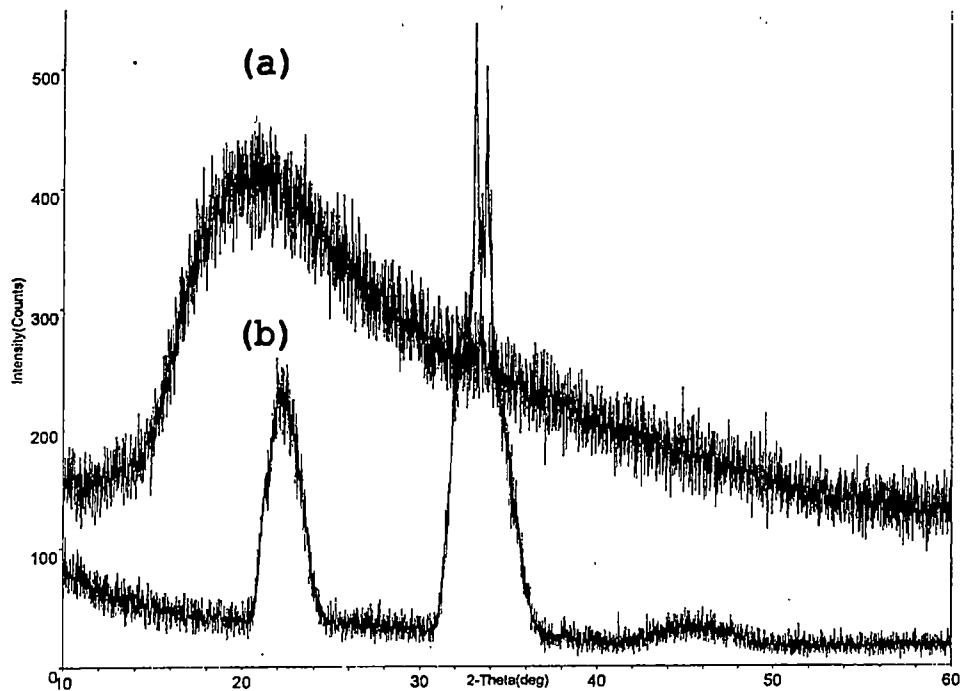


Figure 4. 25 XRD of silicon nitride film deposited with  $E_d = 3 \text{ J/cm}^2$  at room temperature in vacuum(a) and XRD of silicon nitride film deposited with  $E_d = 2.5 \text{ J/cm}^2$  at  $500 \text{ }^\circ\text{C}$  in nitrogen atmosphere(b) ( $1 \sim 2 \times 10^{-3}$  torr).

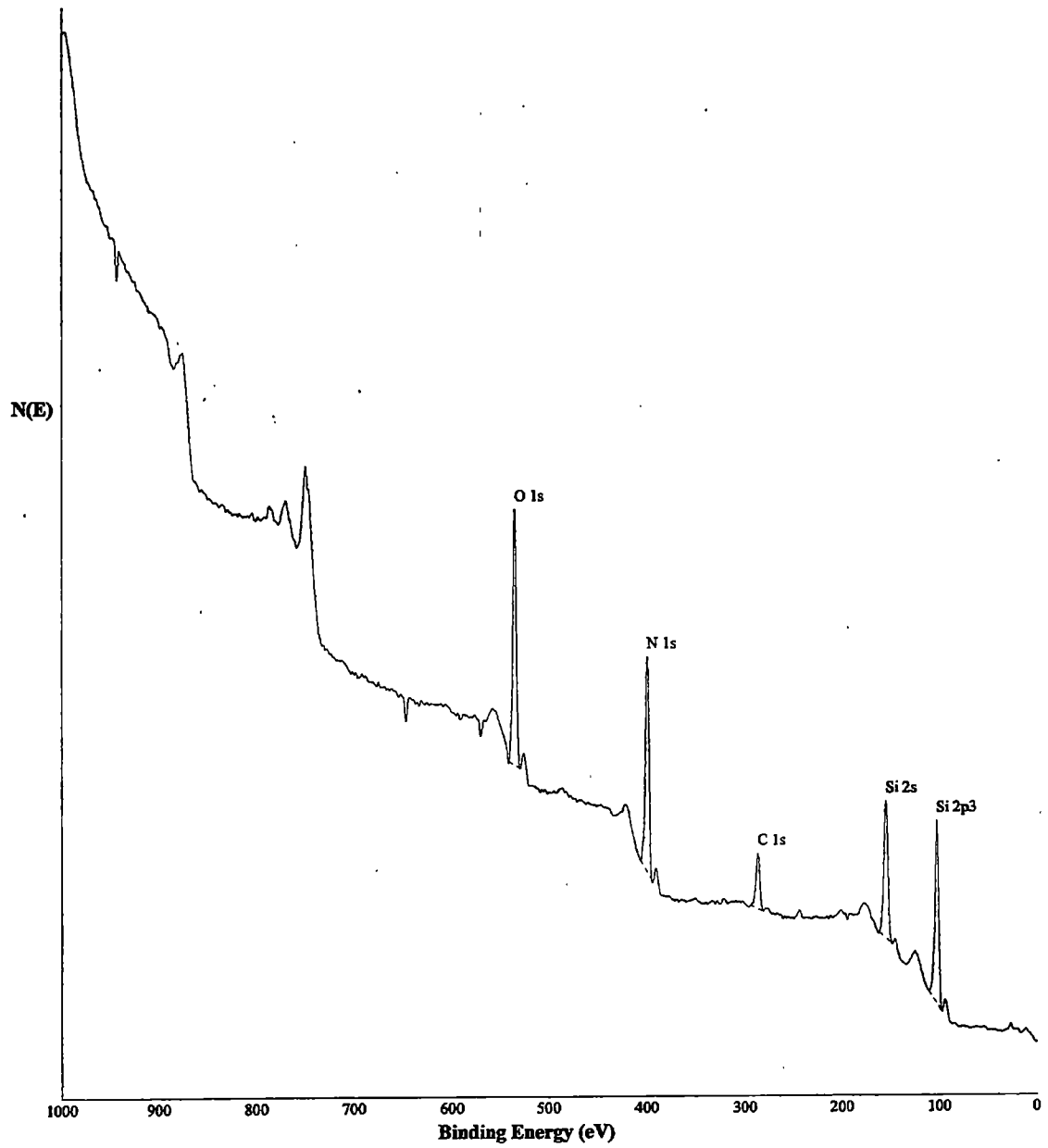


Figure 4. 26. (a) XPS survey spectrum of the silicon nitride film deposited with  $E_d = 2.5\text{ J/cm}^2$  at room temperature in vacuum. The repetition rate was 20 Hz and the target- substrate distance was 4 cm.

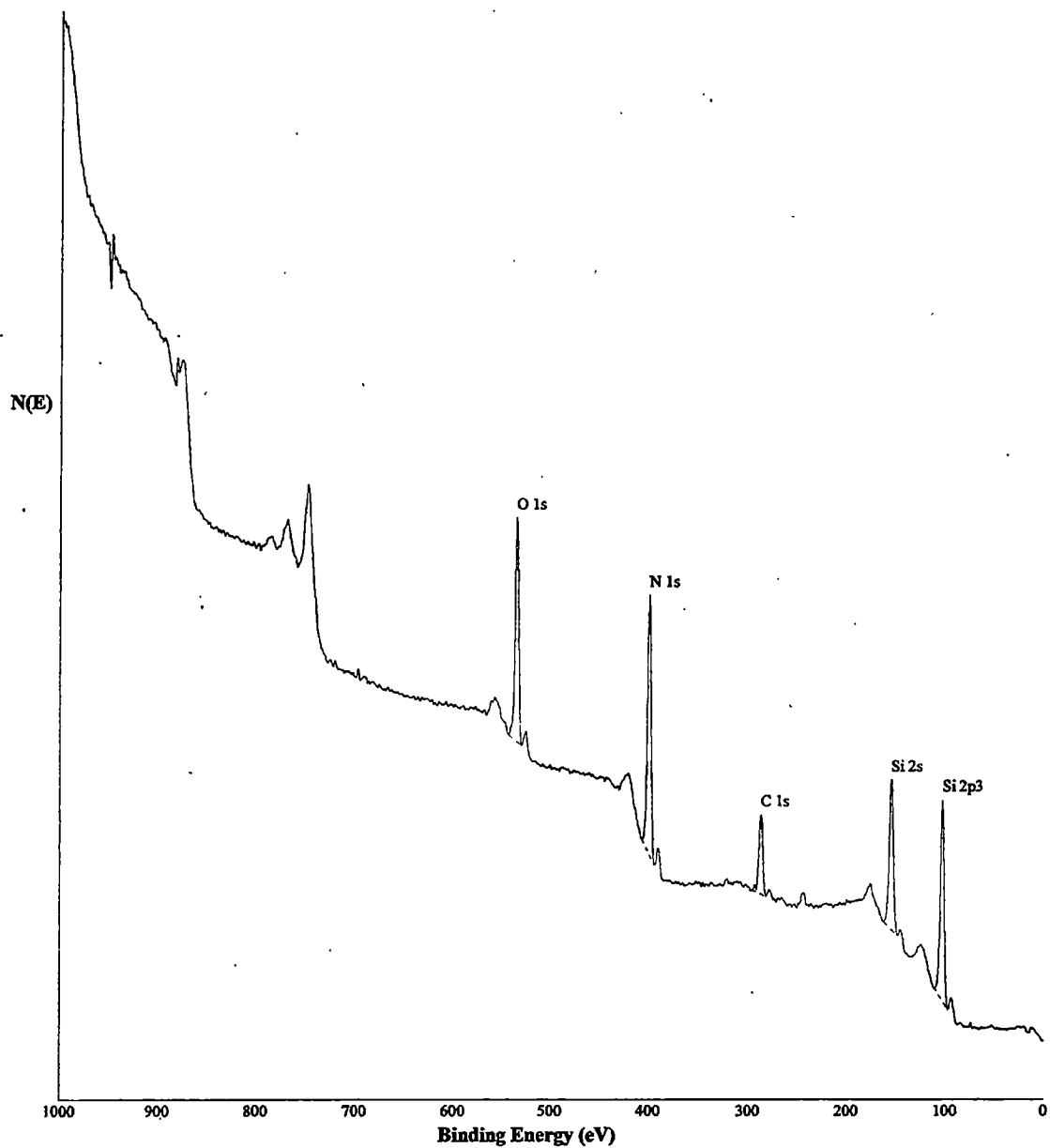


Figure 4. 26. (b) XPS survey spectrum of the silicon nitride film deposited with  $E_d = 2.5 \text{ J/cm}^2$  at  $500 \text{ }^\circ\text{C}$  in  $\text{N}_2$  ( $1 \sim 2 \times 10^{-3} \text{ torr}$ ). The repetition rate was 20 Hz and the target- substrate distance was 4 cm.

Once again the concentration of nitrogen seems to affect the silicon nitride film hardness.

In case of deposition at 500 °C in N<sub>2</sub>, multi-layered film composed of TiN 10 nm + Si<sub>3</sub>N<sub>4</sub> 3 nm having more silicon nitride, which was the hardest hardness in this case, had a higher hardness than that of multi-layered film composed of TiN 10 nm + Si<sub>3</sub>N<sub>4</sub> 1nm containing more titanium nitride, which had the lowest hardness. The hardness of multi-layered film containing more silicon nitride was close to that of silicon nitride film. The limitation imposed on the grain growth of the TiN layer by the intermediate layer of Si<sub>3</sub>N<sub>4</sub> may explain why the TiN 10 nm + Si<sub>3</sub>N<sub>4</sub> 3 nm multi-layered film is significantly harder than TiN film. The increase in hardness of the TiN 10 nm + Si<sub>3</sub>N<sub>4</sub> 3 nm multi-layered film as the temperature increase seems to indicate that the interfacial bonding increases as the temperature increases. The order from the highest to the lowest value of hardness for films deposited in both conditions is completely opposite. It is evident that the hardness of multi-layered films is entirely dependent of the hardness of composing films. In the Table 4. 1 both hardness and elastic modulus are computed for the multi-layer films using a simple rule of mixing. The actual hardness is

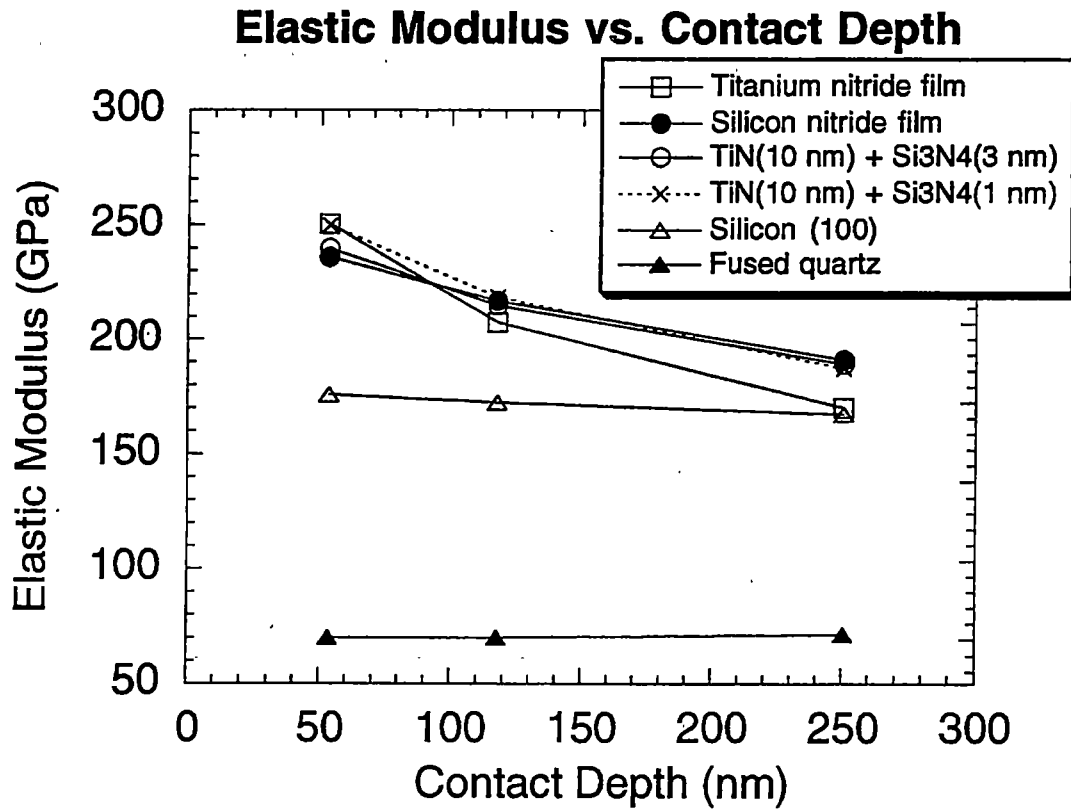


Figure 4. 27 Elastic modulus as a function of contact depth for films deposited at  $E_d = 2.5 \text{ J/cm}^2$ . The repetition rate was 20 Hz and the target-substrate distance was 4 cm. The depositions were performed at 500 °C in nitrogen atmosphere (  $1 \sim 2 * 10^{-3}$  torr ).



higher than that predicted by the rule of mixing in the multilayer films grown at 500 °C. On the other hand the measured values of hardness from multilayer films grown at room temperature are lower than those predicted by the rule of mixing. This is a clear indication that the interfacial bond was weaker when the films were grown at room temperature. This result also indicates that some degree of strength enhancement took place in the TiN 10 nm + Si<sub>3</sub>N<sub>4</sub> 3 nm multi-layered film grown at 500 °C. Figure 4. 27 shows the elastic modulus as a function of contact depth for four samples deposited at 500 °C in nitrogen environment, silicon (100) wafer, and fused quartz. There was no significant difference in values of the elastic modulus for the films. However, titanium nitride film still had the highest elastic modulus around 250 GPa ± 19 that is slightly lower than that of TiN film at room temperature.

S. Veprek and S. Reiprich[37] reported that TiN/Si<sub>3</sub>N<sub>4</sub> composite coating had hardness of 5000 HV and elastic modulus of 500 GPa. These values are twice larger than those obtained in this research. There are several factors that contribute to the hardness of the hard coating. One of these is the effect of the substrate on the measurement. At a certain depth that is shallower than some shallow

critical depth, the hardness measured is the hardness of the film. However, at some deeper than the film thickness, the hardness measured is that of the substrate. At intermediate depths, the hardness measured is some combination of the film and substrate. The substrate influence may partially explain the values of hardness that approach to the value of substrate: 12 GPa for silicon. In order to avoid the effect of the substrate on the hardness measurement of films the film thickness should have been thick enough for nanoindentation.

Elastic effects might be a source of large difference between the hardness obtained by S. Veprek and S. Reiprich[37] and those obtained in this experiment. For the Vickers methods, the hardness is calculated from the indentation area measured after the load is removed.

$$HV = 2 * P * \sin 68^\circ / D^2$$

where D is the mean diagonal of indentation. If significant elastic recovery occurs when the load is withdrawn, the indentation appears much smaller than it was when the load was applied. In this case the hardness measured using underestimated indentation area would be higher than the actual hardness. Since the method developed by Oliver and Pharr[46] using nanoindenter uses the

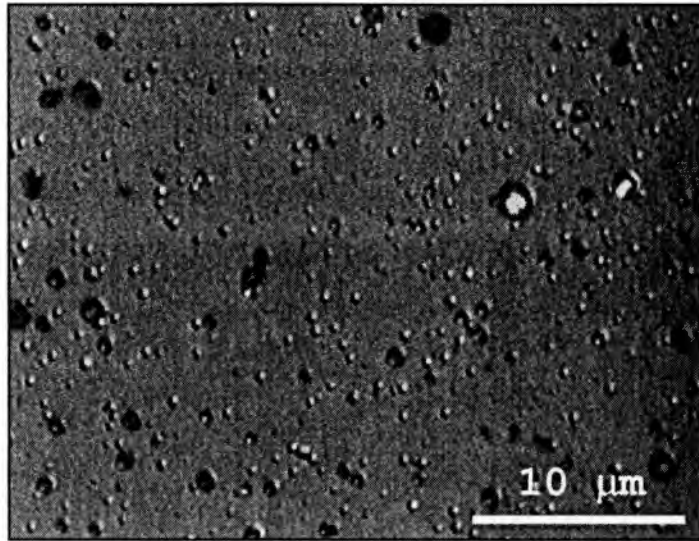
intercept of the initial unloading slope with displacement axis to calculate the contact depth and hence the hardness, it is probably more accurate than the Vickers method. Both silicon wafer and fused quartz were examined to ensure the validity of the nanoindentation technique used in this experiment. The hardness and elastic modulus of silicon and fused quartz agreed quite well with the values in the literature: 12.1 GPa(H) , 176 GPa(E) for silicon and 9.5 GPa, 69 GPa(E) for fused quartz.

Koehler[31] suggested that hardness enhancement can be achieved by forming a structure consisting of a few nanometer thin layers of two materials A and B with a high and low elastic modulus. Also, he mentioned that the critical stress needed to move a dislocation across the interface is proportional to the difference in modulus between the two layers. According to the Koehler's model, a structure consisting of titanium nitride and silicon nitride is a potential candidate for hard coatings because the difference in modulus between the two materials is large; 380 GPa based on the values in literature[28]. However, the differences in elastic modulus between titanium nitride and silicon nitride films deposited in this research were significantly less: 35 GPa at room

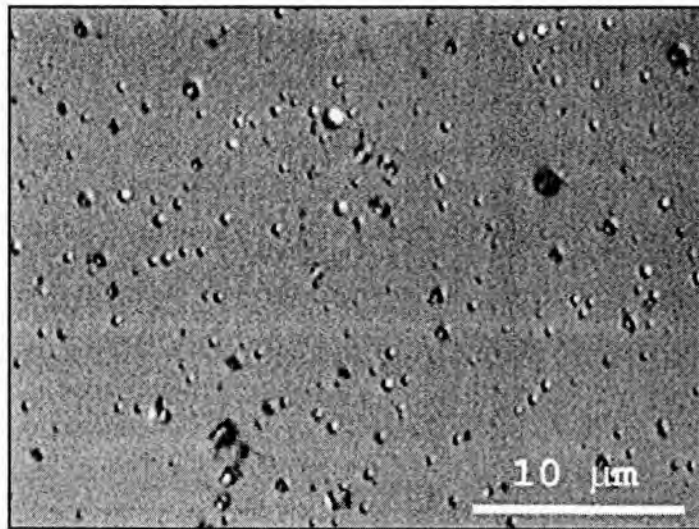
temperature in vacuum and 16 GPa at 500 °C in a nitrogen environment.

As mentioned in the chapter 2, the superlattice period can affect the enhancement of hardness. The maximum hardness of TiN/VN and TiN/NbN films were obtained about 5 and 8 nm of superlattice period[35]. In our studies we used a superlattice period of 11 nm and 13 nm. It is possible that the maximum hardness could be reach at a lower superlattice period. The stress needed to curve a dislocation is inversely proportional to the superlattice period.

Adherence between film and substrate and among films has an effect on the mechanical properties of films. The adherent force depends mainly on properties of film and substrate and deposition technique and parameters used. Particulates produced by energetic pulsed laser ablation probably created something scattering in the nanoindentation measurements. The particulates should be minimized in order to get more reliable data from indentation measurement. Figure 4. 28 shows the micrographs of silicon nitride films grown at room temperature in vacuum(a) and 500 °C in N<sub>2</sub> atmosphere(b). The density of particulates decreased when they were deposited at high



(a)



(b)

Figure 4. 28 Micrographs of silicon nitride film deposited with  $E_d = 2.5 \text{ J/cm}^2$  at room temperature in vacuum(a) and at  $500 \text{ }^\circ\text{C}$  in nitrogen atmosphere(  $1 \sim 2 * 10^{-3} \text{ torr}$ )(b).

temperature in nitrogen atmosphere. The collision between particulates and background gas might reduce the density of particulates. The particulates on both films were uniformly distributed over the whole films. There was no difference in the density and size of particulates for titanium nitride films and multi-layered films.

T. Y. Tsui et al.[55] suggested that the ratio of the hardness to the elastic modulus may be an indicator of resistance to permanent contact damages. The resistance to contact damage is dependent of both the hardness and the elastic modulus of a material because a material having a lower modulus might deform elastically to distribute the load over the larger area resulting in decrease in the contact pressure. Permanent contact damage can be reduced in the materials with the high ratio of the hardness to the elastic modulus. Thus, the titanium nitride film grown at room temperature, which has the highest ratio, is expected to be the most resistant to plastic contact damage.

The data obtained in this experiment regarding the mechanical properties of the films are shown in Table 4. 1 and 4. 2

Table 4. 1 The hardness and elastic modulus of multi-layered films.

Sample	Mechanical Properties	At room temperature in vacuum	At 500 °C in nitrogen ( $10^{-3}$ torr)
Multilayer (TiN 10 nm + Si <sub>3</sub> N <sub>4</sub> 3 nm)	H(GPa)	21 ± 2.3	22 ± 1.8
	Rule of mixing	24.47	19
	E(GPa)	220 ± 21	242 ± 10
	H/E	0.095	0.091
Multilayer (TiN 10 nm + Si <sub>3</sub> N <sub>4</sub> 1 nm)	H(GPa)	24 ± 2.6	19 ± 5
	Rule of mixing	25.73	18.23
	E(GPa)	264 ± 21	248 ± 64
	H/E	0.092	0.075

Table 4. 2 Mechanical properties of films obtained.

Sample	Mechanical Properties	At room	At 500°C
		temperature in vacuum	in nitrogen (10 <sup>-3</sup> torr)
Titanium Nitride	H (GPa)	26 ± 4	18 ± 1
	E (GPa)	265 ± 25	250 ± 19
	H/E	0.100	0.071
Silicon Nitride	H (GPa)	19 ± 0.9	23 ± 0.8
	E (GPa)	230 ± 21	234 ± 9
	H/E	0.081	0.098
Multilayer (TiN 10nm + Si <sub>3</sub> N <sub>4</sub> 3nm)	H (GPa)	21 ± 2.3	22 ± 1.8
	E (GPa)	220 ± 21	242 ± 10
	H/E	0.095	0.091
Multilayer (TiN 10nm + Si <sub>3</sub> N <sub>4</sub> 1nm)	H (GPa)	24 ± 2.6	19 ± 5
	E (GPa)	264 ± 21	248 ± 64
	H/E	0.092	0.075
Silicon	H (GPa)	12.1 ± 0.5	
	E (GPa)	176 ± 10	
Fused Quartz	H (GPa)	9.5 ± 0.3	
	E (GPa)	69 ± 1.8	



## CHAPTER 5

### CONCLUSIONS

1. Titanium nitride films deposited on a (100) silicon substrate by PLD at room temperature with energy density  $E_d = 2.8 \text{ J/cm}^2$  have a randomly oriented polycrystalline microstructure. The crystal structure is with a lattice parameter of 0.426 nm, close to value of bulk titanium nitride. The grain size of this film is in the range of nanometer.
2. Silicon nitride films deposited on a (100) silicon substrate by PLD at room temperature with energy density  $E_d = 2.8 \text{ J/cm}^2$  are amorphous when grown at room temperature. These films are crystalline when the deposition is done at 500 °C in  $\text{N}_2$ .
3. The density and size of the particulates on the silicon nitride film grown at room temperature increase with increasing laser energy density and decreasing target-substrate distance. Film deposited at a target-substrate distance of 2 cm has very large residual stress that promotes fractures in different region. The

deposition rate is inversely proportional to the target-substrate distance.

4. Cone morphology is developed on the silicon nitride target after irradiation with  $E_d = 2.5 \text{ J/cm}^2$  for 25,000 shots of pulse. The cones produced are aligned along the direction of incident beams. The ablated target has less nitrogen than the as-received target.
5. Titanium nitride film deposited at room temperature has a hardness of 26 GPa, which is higher than that of bulk TiN[28], and elastic modulus of 265 GPa, which is about half of that of bulk TiN[28].
6. Of all the films grown at room temperature silicon nitride has the lowest hardness; 19 GPa.
7. In case of deposition at room temperature in vacuum the TiN 10 nm + Si<sub>3</sub>N<sub>4</sub> 1 nm multi-layered film has a higher hardness than the TiN 10 nm + Si<sub>3</sub>N<sub>4</sub> 3 nm multi-layered film. The hardness of both films are lower than the hardness predicted by the rule of mixing.

8. The elastic moduli of titanium nitride and multi-layered(combination of TiN 10 nm + Si<sub>3</sub>N<sub>4</sub> 1 nm) films are almost the same; 265 GPa for TiN and 264 GPa for multi-layered film.
9. Titanium nitride film grown at room temperature has more nitrogen content than titanium nitride film grown at 500 °C in nitrogen atmosphere. The hardness and elastic modulus of titanium nitride film deposited at 500 °C are 18 GPa and 250 GPa, respectively that are lower than those of titanium nitride film deposited at room temperature.
10. Silicon nitride film grown at 500 °C has the highest hardness among films grown at that temperature and background gas. Silicon nitride at 500 °C in a N<sub>2</sub> environment has more nitrogen content than silicon nitride at room temperature in vacuum.
11. Of the two multilayer films grown at 500 °C the one that contains more silicon nitride is the harder. The hardness of the TiN 10 nm + Si<sub>3</sub>N<sub>4</sub> multi-layered film is

higher than the hardness predicted by the rule of mixing.

12. For every deposition condition the elastic modulus differences between titanium nitride and silicon nitride films are significantly smaller than what we expected on the basis of the values for bulk materials.
13. The particulate density on the silicon nitride film grown at 500 °C in nitrogen environment is lower than that on the silicon nitride film grown at room temperature in vacuum.
14. The titanium nitride film deposited at room temperature in vacuum might have the strongest resistance to permanent contact damage according to the ratio of the Hardness to the elastic modulus (  $H / E = 0.1$  ).

## REFERENCES

1. M. Wittmer, *J. Vac. Sci. Technol.* **A3**, 1797 (1985).
2. T. Itoh, *ion Beam Assisted Film Growth*, Elsevier, Amsterdam (1989).
3. A. Valentini, F. Quaranta, M. Penza, L. Vasanelli, and G. Battaglin, *J. Appl. Phys.* **69**, 7360 (1991).
4. A. J. Perry, *J. Vac. Sci. Technol.* **A8**, 3186 (1990).
5. F. H. M. Sanders and G. Verspui, *Thin Solid Films*, **161**, L87 (1988).
6. E. w. Kreutz, M. Krosche, H. Sung, and A. Voss, *Appl. Surf. Sci.* **54**, 69 (1992).
7. D. Craciun and V. Craciun, *Appl. Surf. Sci.* **54**, 75 (1992).
8. J. C. S. Kools, C. J. C. M. Nillesen, S. H. Brongersma, E. Van der Riet, and J. Dieleman, *J. Vac. Sci. Technol.* **A10**, 1809 (1992).
9. J. Narayan, P. Tiwari, X. Chen, J. Singh, R. Chowdhury, and T. Zhelva, *Appl. Phys. Lett.* **61**, 1290 (1992).
10. R. Chowdhury, R. D. Vispute, K. Jagannadham, and J. Narayan, *J. Mater. Res.* **11**, 1458 (1996).
11. N. Biunno, J. Narayan, S. K. Hofmeister, A. R. Srivatsa, and R. K. Singh, *Appl. Phys. Lett.* **54**, 1519 (1989).
12. A. Kumar, H. L. Chan, and M. Shamsuzzoha, *Hard Coating Based on Borides, Carbides, & Nitrides*, edited by A. Kumar, Y. W. Chung, and R. W. J. Chia, TMS, 219 (1998).

13. I. N. Mihailescu, A. Lita, V. S. Teodorescu, A. Luches, M. Martino, A. Perrone, and M. Garter, *J. Vac. Sci. Technol.* **A14**, 2839 (1996).
14. X. Xu, K. Seki, N. Chen, H. Okabe, J. M. Frye, and J. B. Halpern, *Mat. Res. Symp. Proc.* **285**, 331 (1993).
15. E. Fogarassy, C. Fuchs, A. Slaoui, S. de Unamuno, J. P. Stoquert, W. Marine, and B. Lang, *J. Appl. Phys.* **76**, 2612 (1994).
16. D. J. Elliott, *Ultraviolet Laser Technology and Applications*, Academic Press, (1995).
17. W. W. Duley, *UV Laser: effect and applications in materials science*, Cambridge University Press, (1996).
18. J. T. Cheung, *Pulsed Laser Deposition of Thin Films*, edited by D. B. Chrisey and G. K. Hubler, John Wiley & Sons, (1994).
19. J. E. Greene, *Multicomponent and Multilayered Thin Films for Advanced Microtechnologies*, edited O. Auciello and J. Engemann, Kluwer Academic Publishers, NATO/ASI Series **E234**, 39 (1993).
20. D. H. Lowndes, *Experimental Methods in the Physics Sciences*, **30**, 475 (1998).
21. L. C. Chen, *Pulsed Laser Deposition of Thin Films*, edited by D. B. Chrisey and G. K. Hubler, John Wiley & Sons, (1994).
22. D. H. A. Blank, R. P. J. Ijsselsteijn, P. G. Out, H. J. H. Kuiper, J. Floksura, and H. Rogalla, *Mater. Sci. Eng.* **B13**, 67 (1992).

23. W. Kautek, B. Roas, and L. Schultz, *Thin Solid Films* **191**, 317 (1990).
24. A. Matsunawa, S. Katayama, A. Suzuki, and T. Ariyasu, *Trans. J. Welding Res. Inc.* **15**, 61 (1986).
25. D. H. Lowndes, C. M. Rouleau, D. B. Geohegan, A.A. Poretzky, M. A. Strauss, A. J. Pedraza, J. W. Park, J. D. Budai, and D. B. Poker, Pulsed laser ablation growth and doping of epitaxial compound semiconductor films, in press.
26. K. L. Saenger, *Pulsed Laser Deposition of Thin Films*, edited by D. B. Chrisey and G. K. Hubler, John Wiley & Sons, (1994).
27. A. A. Gorbunov and V. I. Konov, *Sov. Phys. Tech. Phys.* **34**, 77 (1989).
28. H. Holleck, *J. Vac. Sci. Technol.* **A6**, 2661 (1986).
29. H. Holleck, Ch. Kuhl, and H. Schulz, *J. Vac. Sci. Technol.* **A3**, 2345 (1985).
30. R. W. K. Honeycome, *Plastic deformation of Metals*, 2nd edn., Edward Arnold, London (1984).
31. J. S. Koehler, *Phys. Rev.* **B2**, 547 (1970).
32. D. Tabor, *J. Inst. Met.* **79**, 1 (1951).
33. U. Helmesson, S. Todorova, S. A. Barnett, J. E. Sundgren, L. C. markert, and J. E. Greene, *J. Appl. Phys.* **62**, 481 (1987).
34. M. Shinn, L.Hultman, and S. A. Barnett, *J. Mater. Res.* **7**, 901 (1992).
35. X. Chu and S. A. Barnett, *J. Appl. Phys.* **77**, 4403

- (1995).
36. P. B. Mirkarimi, L. Hultman, and S. A. Barnett, *Apply. Phys. Lett.* **57**, 2654 (1990).
  37. S. Veprek and S. Reiprich, *Thin Solid Films* **268**, 64 (1995).
  38. S. Veprek, *Thin Solid Films* **297**, 145 (1997).
  39. S. Veprek, S. Reiprich, and Li Shizhi, *Appl. Phys. Lett.* **66**, 2640 (1995).
  40. S. Veprek, M. Haussmann, and S. Reiprich, *J. Vac. Sci. Technol.* **A14**, 46 (1996).
  41. R. W. Hertzberg, *Deformation and Fracture Mechanics of Engineering Materials*, 3<sup>rd</sup>. edn., Wiley, New York (1989).
  42. A. Kelly and N. H. MacMillan, *Strong Solid*, 3<sup>rd</sup>. edn., Clarendon, Oxford (1986).
  43. D. Tabor, *Proc. R. Soc.* **A192**, 247 (1948).
  44. S. I. Bulychev and V. P. Alekhin, *Zavod. Lab.* **53**, 76 (1987).
  45. J. B. Pethica, R. Hutchings, and W. C. Oliver, *Philos. Mag.* **A48**, 593 (1983).
  46. W. C. Oliver and G. M. Pharr, *J. Mater. Res.* **7**, 1564 (1992).
  47. I. N. Sneddon, *Int. J. Engng. Sci.* **3**, 47 (1965).
  48. M. Ohring, *The Materials Science of Thin Films*, Academic Press Inc., San Diego, CA (1992).
  49. P. E. Dyer, R. D. Greenough, A. Issa, and P. H. Key, *Apply. Surf. Sci.* **43**, 387 (1989).



50. M. A. George, J. J. Weimer, and A. Kumar, *Hard Coating Based on Borides, Carbides & Nitrides*, edited by A. Kumar, Y. W. Chung, & R. W. J. Chia, TMS, 203 (1998).
51. E. Hontzopoulos and E. damigos, *Appl. Phys.* **A52**, 421 (1991).
52. I. Miyamoto and H. Maruo, *SPIE* **1279**, 66 (1990).
53. G. M. Ingo and N. Zacchetti, *High Temperature Science*, **28**, 137 (1990).
54. I. N. Mihailescu, A. Lita, V. S. Teodorescu, A. Luches, M. Martino, A. Perrone, and M. Gartner, *J. Vac. Sci. Technol.* **A14**, 2839 (1996).
55. T. Y. Tsui, G. M. Pharr, W. C. Oliver, Y. W. Chung, E. C. Cutionggo, C. B. Bhatia, R. L. White, R. L. Rhoades, and S. M. Gorbatskin, *Mat. Rec. Symp. Proc.* Vol. **356**, 767 (1995).

## VITA

Won-Seok Kim was born in Seoul, Korea on February 13, 1972. After graduating from high school, he entered the Kangwon National University in March 1990. After serving two years in the Korean Army, he received a Bachelor of Engineering degree with a major in Materials Science & Engineering in February 1996.

In January 1997, he joined the University of Tennessee, Knoxville, Materials Science & Engineering for working towards his Masters of Science degree. He plans to continue his study for Ph.D. degree in the Department of Materials Science & Engineering at the University of Florida, Gainesville.

He is a member of ASM International and TMS.